Research Square

Preprints are preliminary reports that have not undergone peer review.
They should not be considered conclusive, used to inform clinical practice,
or referenced by the media as validated information.

# Time-Domain Simulation using Component Mode Synthesis for a Piano

**Eiji Tominaga**

eiji.tominaga@music.yamaha.com

Yamaha Corporation

**Masanao Sato**

Yamaha Corporation

**Research Article**

**Keywords:** piano, physical modeling, time-domain simulation, vibroacoustics, component mode synthesis (CMS), finite element method (FEM), fast multipole boundary element method (FMBEM), nonlinear eigenvalue analysis, geometrical nonlinearity, manufacturing-induced residual stress

**Posted Date:** April 6th, 2026

**DOI:** https://doi.org/10.21203/rs.3.rs-9307819/v1

**License:** This work is licensed under a Creative Commons Attribution 4.0 International License.
Read Full License

**Additional Declarations:** No competing interests reported.

# Time-Domain Simulation using Component Mode Synthesis for a Piano

Eiji Tominaga[1*] and Masanao Sato[1]

[1*]Research and Development Division, YAMAHA CORPORATION, 10-1 Nakazawa-cho, Chuo-ku, Hamamatsu, 430-8650, Shizuoka, Japan.

*Corresponding author(s). E-mail(s): eiji.tominaga@music.yamaha.com;
Contributing authors: masanao.sato@music.yamaha.com;

**Abstract**

We present a physics based, time-domain numerical simulation framework that treats a full-scale grand piano as a comprehensively coupled vibroacoustic system, encompassing nonlinear hammer–string interaction, geometrically nonlinear and lossy strings with anisotropic end supports, a three dimensional orthotropic wooden body with structural damping, and exterior acoustic radiation. The approach combines hybrid interface component mode synthesis (CMS) and Galerkin method for the strings with a finite element (FE) body model and a fast multipole boundary element method (FMBEM) for the surrounding air. The large coupled body–air subsystem is reduced via a complex mode CMS based on nonlinear eigenvalue analysis, yielding complex modal parameters at string support locations together with transfer functions to virtual microphones for efficient auralization. Manufacturing-induced residual stresses are explicitly incorporated through nonlinear static analysis of the assembly process, enabling system level causal links from design and fabrication parameters to radiated sound. To our knowledge, this work represents the first fully integrated time-domain piano simulation that simultaneously couples: (i) a nonlinear, double layer generalized Maxwell model of hammer felt; (ii) a spatial, bidirectionally coupled string model with stiffness, dispersion, and zig-zag/anisotropic boundary conditions at bridge and bearing; and (iii) a 3D body–air model reduced by complex modal synthesis, including residual stress effects. The method reconstructs driving point mobilities and perceptually salient phenomena—partial dispersion, polarization exchange, and "ringing"—and provides audible examples as supplementary material. Beyond piano acoustics, the pipeline constitutes a generalizable methodology for large scale, strongly coupled nonlinear structural–acoustic simulations in engineering design, enabling parameter sensitive, time-domain auralization with tractable cost.

**Keywords:** piano, physical modeling, time-domain simulation, vibroacoustics, component mode synthesis (CMS), finite element method (FEM), fast multipole boundary element method (FMBEM), nonlinear eigenvalue analysis, geometrical nonlinearity, manufacturing-induced residual stress

# 1 Introduction

Achieving an ideal piano tone requires identifying an optimal combination of design parameters across the entire instrument, which constitutes a highly complex, large-scale vibroacoustic system. Traditional empirical approaches—heavily dependent on craftsmanship, experience, and iterative prototyping—are often inefficient due to the large number of interacting variables and unavoidable uncertainties arising from natural material variation and manual adjustment. These limitations make it difficult to systematically evaluate how specific structural and acoustic factors influence the resulting sound. To address this challenge, physics-based modeling and numerical simulation have emerged as promising tools for understanding and predicting the mechanisms of piano sound production.

A substantial body of research on physical modeling of piano components has been accumulated over several decades. Early studies focused on simplified interactions such as the coupling between a linear string and a linear bridge, solved via analytical techniques including Laplace transforms [1]. Subsequent work addressed the nonlinear hammer–string interaction [2], the hysteretic behavior of hammer felt [3], and the generation of longitudinal string vibration [4]. More recently, high-fidelity time-domain simulations have incorporated two-dimensional and three-dimensional models of the soundboard and surrounding air [5]. While each of these studies contributed valuable insights into individual subsystems, none provided a complete representation of the piano as an integrated acoustic instrument. In particular, previous approaches often simplified essential elements such as geometrical nonlinearity, string end-support anisotropy, wood orthotropy, manufacturing-induced residual stresses, and the three-dimensional coupling between the body and exterior acoustics.

From the perspective of piano design and engineering practice, ignoring these factors is not acceptable when the goal is to clarify the causal relationship between design specifications and the resulting sound. Based on the authors' experience in piano development, the following factors (a)–(i) are indispensable for accurate sound prediction:

(a) nonlinear viscoelastic compression of hammer felt;
(b) spatial string vibration including stiffness, losses, and geometrical nonlinearity;
(c) rear duplex segments;
(d) three-dimensional complex orthotropic elasticity of wooden components;
(e) inclusion of nearly all structural elements, such as soundboard, ribs, bridge, rim, key bed, cast-iron frame, legs, casters, and top lid;
(f) manufacturing-induced residual stresses arising from successive gluing, bolting and stringing processes;

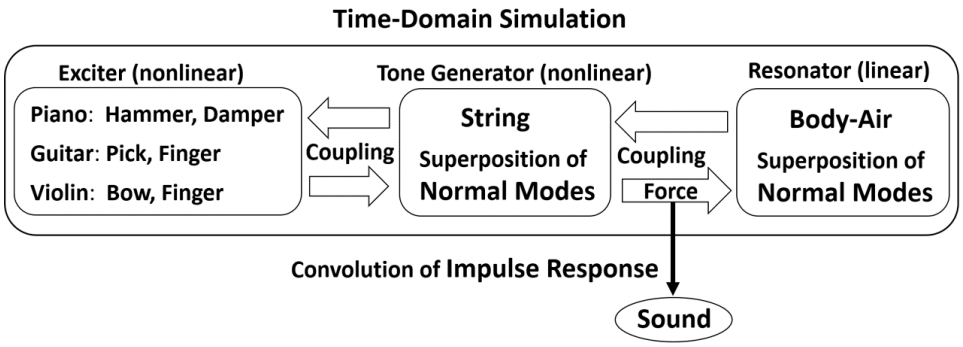



**Fig. 1** Block diagram of the proposed sound-synthesis framework for string instruments (e.g., piano, guitar, and violin).

(g) three-dimensional body–air coupling with non-proportional damping;
(h) anisotropic end-support conditions of strings; and
(i) acoustic radiation from all surfaces of the piano into an open field.

A piano that incorporates all of these factors forms a highly intricate system, characterized as a three-dimensional coupled structure involving nonlinear subsystems (hammers and strings) and a large-scale linear vibroacoustic subsystem (body and air). Direct time-domain simulation of such a system is computationally prohibitive due to its immense dimensionality. To overcome this challenge, we employ an advanced CMS-based reduction strategy that enables efficient treatment of large-scale exterior vibroacoustic problems—an application of CMS far less explored than conventional interior structural dynamics [6].

Depending on the characteristics of each substructure, we adopt appropriate CMS formulations (free-interface, fixed-interface, and hybrid-interface) to model interactions among the strings, body, and surrounding air. The normal modes of the coupled body–air system are obtained through a nonlinear eigenvalue analysis combined with the fast multipole boundary element method (FMBEM), and are orthogonalized into complex modes for time-domain use. These reduced modal parameters allow us to synthesize sound by convolving the impulse response between string support points and virtual microphone positions with string forces computed in the time domain. The block diagram of the proposed sound synthesis method is shown in Fig. 1. Notably, this block diagram differs crucially from the well-known block diagram of [7]: the traditional block diagram ignores the feedback from the linear resonator (body–air system) to the strings, whereas ours takes this feedback into account. As shown in this figure, the basic idea of the presented method can be applied to other musical instruments, such as guitars and violins. These stringed instruments share the property that they can be modeled as a coupled system consisting of nonlinear exciters (such as hammers, a pick, or a bow), nonlinear strings, a linear body, and linear air.

The remainder of this paper is organized as follows. Section 2 presents the physical models and governing equations of each subsystem and the fully coupled system. Section 3 describes the numerical procedures, including eigenvalue analysis, modal reduction, and time-domain integration. Section 4 provides simulation results with

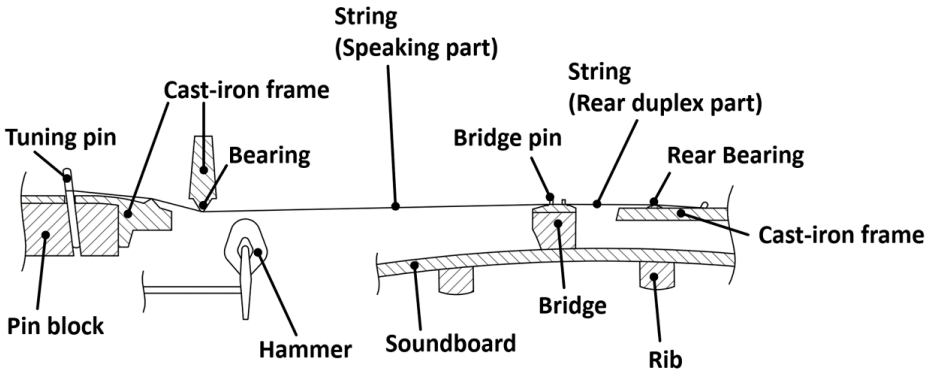



**Fig. 2** Schematic diagram of the main structural components of a grand piano.

audible examples, and Section 5 discusses the physical implications of the findings. Section 6 concludes the study and outlines possible directions for future work.

# 2 Model and governing equations

First, we define the coordinate axes. For the object coordinates (the global coordinates) of the body, the right-handed Cartesian coordinates $(X, Y, Z)$ are used. In the case of a grand piano, the $XY$-plane is usually parallel to the floor on which the piano is placed, with the $X$-axis from the bass side to the treble side, the $Y$-axis from the player side to the piano side, and the $Z$-axis vertically upward. The strings of a grand piano have the speaking, rear duplex, and other parts, as shown in Fig. 2. Notably, herein, the "string" includes only the speaking and rear duplex parts, and the remaining parts are included in the "body". For the object coordinates (the local coordinates) of the string at rest, the right-handed Cartesian coordinates $(x, y, z)$ corresponding to each part are used. The $x$-axis aligns with the chord in the string-axis direction, the $y$-axis is set parallel to the $XY$-plane, and the $z$-axis is almost vertically upward. In the speaking part, the $x$-axis is defined as $x = -l^{[1]}$ at the end-support on the cast-iron frame, i.e., bearing (including agraffes) and $x = l^{[1]}$ at the end-support on the bridge. The $y$-axis goes from the treble side to the bass side. Conversely, in the rear duplex part, the $x$-axis is defined as $x = -l^{[2]}$ at the end-support on the cast-iron frame, i.e., rear bearing and $x = l^{[2]}$ at the end-support on the bridge, and the $y$-axis goes from the bass side to the treble side. Here, $l^{[i_L]} = L^{[i_L]}/2$. $L^{[i_L]}$ $(i_L = 1, 2)$ are the lengths of the parts of the string at rest, where $i_L = 1$ and $i_L = 2$ denote the speaking and rear duplex parts, respectively.

## 2.1 Hammer

Pianos produce a soft tone that contains almost no high-frequency components when struck lightly and a powerful tone that contains many high-frequency components when struck strongly. This is mainly due to the nonlinear viscoelasticity of the hammer felt.

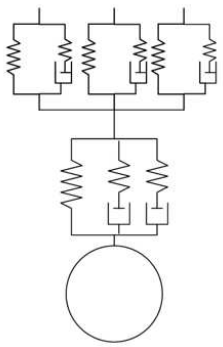


**Fig. 3** Hammer model consisting of a lumped mass and a double-layer nonlinear generalized Maxwell model ($I_W = 3, I_{Hb} = 2$)

In viscoelastic theory, the Maxwell and Voigt models are the most basic. The former comprises a spring and a dashpot connected in series, whereas the latter comprises a spring and a dashpot connected in parallel. The generalized Maxwell model, which combines one spring and one or more Maxwell models in parallel, is a practical model for expressing linear viscoelasticity [8]. Furthermore, by replacing the compression $w$ (where $w$ is a non-negative real number) in the expression of this linear model with $w^p$ (where $p$ is a positive real number), the nonlinear generalized Maxwell model can be obtained. The hammer felt model with nonlinear hysteresis proposed by Stulov is a type of nonlinear generalized Maxwell model [3]. This paper proposes a double-layer nonlinear generalized Maxwell model that more accurately represents the dynamic compression characteristics of hammer felt (Fig. 3). The upper and lower layer of this model represent the viscoelasticity of "the hammer tips that contact each string" and "the hammer core", respectively.

When using the lumped mass model with the assumption that the hammer moves on one axis, the equation of motion of the hammer is expressed as follows:

$$M_H \ddot{u}_H(t) = -f_{Hb}(t) \tag{1}$$

where $M_H$ is the hammer mass, $u_H(t)$ is the displacement of the hammer mass, and $f_{Hb}(t)$ is the force exerted by the hammer mass on the lower layer of the hammer felt. $t$ is time, and an overdot denotes differentiation with respect to time. The equation of equilibrium on the joint point of the upper and lower layers is expressed as follows:

$$f_{Hb}(t) = \sum_{i_W=1}^{I_W} f_{Ha}^{[i_W]}(t) \tag{2}$$

where $f_{Ha}^{[i_W]}(t)$ is the force exerted by the upper layer of the hammer felt on the string, and $i_W$ and $I_W$ are the index and number of strings corresponding to a certain key, respectively. When using the nonlinear generalized Maxwell model with the assumption that the hammer felt deforms only in the direction of the hammer motion, the

force–compression relational expressions for the upper and lower layers of the hammer felt are given as follows:

$$f_{Ha}^{[i_W]}(t) = K_{Ha}^{[i_W]}\left[1 - \beta_{Ha}^{[i_W]} + \frac{\beta_{Ha}^{[i_W]}}{D + 1/\tau_{Ha}^{[i_W]}}D\right]\{\, w_{Ha}^{[i_W]}(t)\,\}^{p_{Ha}^{[i_W]}} \tag{3a}$$

$$f_{Hb}(t) = K_{Hb}\left[1 - \sum_{i_{Hb}=1}^{I_{Hb}} \beta_{Hb}^{[i_{Hb}]} + \sum_{i_{Hb}=1}^{I_{Hb}} \frac{\beta_{Hb}^{[i_{Hb}]}}{D + 1/\tau_{Hb}^{[i_{Hb}]}}D\right]\{\, w_{Hb}(t)\,\}^{p_{Hb}} \tag{3b}$$

where $D\,(= d/dt)$ is a differential operator, $w_{Ha}^{[i_W]}(t)$ and $w_{Hb}(t)$ are the compression of the hammer felt, $K_{Ha}^{[i_W]}$ and $K_{Hb}$ are the stiffness coefficients, $p_{Ha}^{[i_W]}$ and $p_{Hb}$ are the positive real numbers representing nonlinearity, $\tau_{Ha}^{[i_W]}$ and $\tau_{Ha}^{[i_{Hb}]}$ are the relaxation times, and $\beta_{Ha}^{[i_W]}$ and $\beta_{Hb}^{[i_{Hb}]}$ are the positive real numbers with $\beta_{Ha}^{[i_W]} < 1$ and $\sum_{i_{Hb}=1}^{I_{Hb}} \beta_{Hb}^{[i_{Hb}]} < 1$. The subscripts $_{Ha}$ and $_{Hb}$ denote the upper and lower layers of the hammer felt, respectively. $i_{Hb}$ and $I_{Hb}$ are the index and number of the spring–dashpot element (i.e., Maxwell model) in the lower layer, respectively.

When the hammer tip contacts the string surface, the integral type of the force–compression relational expression of the upper layer is derived from Eq. (3a) as follows, incorporating the displacement of the string:

$$f_{Ha}^{[i_W]}(t) = K_{Ha}^{[i_W]}\left[\{\, w_{Ha}^{[i_W]}(t)\,\}^{p_{Ha}^{[i_W]}} + \int_0^t \{\, w_{Ha}^{[i_W]}(t-\tau)\,\}^{p_{Ha}^{[i_W]}}\left\{-\frac{\beta_{Ha}^{[i_W]}}{\tau_{Ha}^{[i_W]}} exp\big(-\frac{\tau}{\tau_{Ha}^{[i_W]}}\big)\right\} d\tau\right] \tag{4}$$

$$\text{with} \quad f_{Ha}^{[i_W]}(t) \geqq 0, \quad w_{Ha}^{[i_W]}(t) = u_{Hab}(t) - \sum_{s=z,x,y} u_s(x_H^{[i_W]}, t)\, e_{Hs} \;\geqq 0$$

where $u_{Hab}(t)$ is the displacement of the joint part of the upper and lower layers, $u_s(x,t)$ the $s$-direction component of the string displacement $(s = z, x, y)$, and $x_H^{[i_W]}$ the $x$ coordinate of the striking point. $e_{Hz} = \cos\varphi_1 \cos\varphi_2$, $e_{Hx} = \sin\varphi_1$, $e_{Hy} = \cos\varphi_1 \sin\varphi_2$, where $\varphi_1$ is the angle obtained by subtracting "the angle of the hammer-motion direction from the $x$-axis" from the right angle, and $\varphi_2$ is the angle that "the plane, including the hammer-motion direction and the $x$-axis," makes with the $z$-axis. The recovery amount of the felt compression of the upper layer after the hammer tip leaves the string is obtained by solving the linear homogeneous ordinary differential equation with respect to $\{\, w_{Ha}^{[i_W]}(t)\,\}^{p_{Ha}^{[i_W]}}$, which is obtained by replacing $f_{Ha}^{[i_W]}(t)$ in Eq. (3a) with 0.

Similarly, when at least one hammer tip contacts the string of a certain key, i.e., when at least one string of the certain key contacts the hammer, the integral type of the force–compression relational expressions of the lower layer is derived from Eq. (3b)

as follows, incorporating the displacement of the hammer mass:

$$f_{Hb}(t) = K_{Hb}\left[\{\, w_{Hb}(t)\,\}^{p_{Hb}} + \int_0^t \{\, w_{Hb}(t-\tau)\,\}^{p_{Hb}} \sum_{i_{Hb}=1}^{I_{Hb}} \left\{ -\frac{\beta_{Hb}^{[i_{Hb}]}}{\tau_{Hb}^{[i_{Hb}]}} exp\big(-\frac{\tau}{\tau_{Hb}^{[i_{Hb}]}}\big) \right\} d\tau \right] \tag{5}$$

$$\text{with} \quad f_{Hb}(t) \geqq 0, \quad w_{Hb}(t) = u_H(t) - u_{Hab}(t) \ \geqq 0$$

The recovery amount of felt compression of the lower layer after all the hammer tips leave the strings of a certain key is obtained by solving the linear homogeneous ordinary differential equation with respect to $\{\, w_{Hb}(t)\,\}^{p_{Hb}}$, which is obtained by replacing $f_{Hb}(t)$ in Eq. (3b) with 0.

## 2.2 Strings

This subsection formulates a three-dimensional geometrically nonlinear string model with anisotropic end supports, enabling accurate reproduction of string polarization exchange and ringing phenomena.

In the range below nearly the 40th key (the C4 note) of a standard 88-key piano, sounds like a bell ringing or sharp, metallic sounds are frequently heard. These distinct nonharmonic sounds, which are often referred to as the "ringing sound", become more prominent when the string is struck hard. If the level of the ringing sounds is too high, then it can be perceived as unpleasant, whereas if there are no such sounds at all, then the piano sound would be monotonous and uninteresting. Therefore, it is desirable to design the ringing sounds to be moderately audible. The analysis of the ringing sounds of a piano led to the discovery of the following phenomena: (a) In piano partial series, there is a subseries whose frequency deviations from the harmonic series are nearly 1/4 of that of the main series [9]. (b) When "the frequency of the odd-order partials of the subseries" matches "the odd-order natural frequency of the longitudinal vibration of the string," or when "the frequency of the even-order partials of the subseries" matches "the even-order natural frequency of the longitudinal vibration of the string," the level of the partials of the subseries, i.e., the ringing sound, increases. More analytically, (b') When "the sum of the odd-order and the even-order natural frequencies of the transverse vibration of the string" matches "the odd-order natural frequency of the longitudinal vibration of the string," or when "the sum of a set of the odd-order natural frequencies" or "the sum of a set of the even-order natural frequencies of the transverse vibration of the string" matches "the even-order natural frequency of the longitudinal vibration of the string," the ringing sound increases [10].

These phenomena, which have been experimentally confirmed, can be explained using the string model, which incorporates stiffness and geometrical nonlinearity under the simplification that "the coupling between the transverse vibration and longitudinal vibration is unidirectional [4]." However, models with such simplification do not satisfy the energy conservation law based on Newton's laws. Therefore, to obtain an appropriate solution that satisfies this law, a nonlinear string model incorporating the bidirectional coupling should be employed [5]. Furthermore, to quantitatively simulate piano sounds, including the ringing sound, with higher precision, it is crucial to

model the mechanism of 3D coupling between the spatial string and the string support ends on the body (bridge and bearing), in addition to the elements considered in previous studies. Herein, a spatial string with losses, stiffness, and geometrical nonlinearity and the 3D coupling between the string and the string support ends on the body–air system are precisely described.

Considering the initial strain and geometrical nonlinearity of the Timoshenko beam model, the strain–displacement relationship of a string can be expressed as follows:

$$\varepsilon_x(x,t) = \varepsilon_0 + \left\{ \left(1+\frac{\partial}{\partial x}u_x\right)^2 + \left(\frac{\partial}{\partial x}u_y\right)^2 + \left(\frac{\partial}{\partial x}u_z\right)^2 \right\}^{\frac{1}{2}} - z\,\frac{\partial}{\partial x}\psi_z(x,t) - y\,\frac{\partial}{\partial x}\psi_y(x,t) - 1$$

$$\gamma_{xz}(x,t) = -\psi_z(x,t) + \frac{\partial}{\partial x}u_z(x,t),\ \gamma_{xy}(x,t) = -\psi_y(x,t) + \frac{\partial}{\partial x}u_y(x,t)$$

where $\varepsilon_x(x,t)$ is the normal strain of the string, $\varepsilon_0$ is the initial normal strain, $\gamma_{xz}(x,t)$ and $\gamma_{xy}(x,t)$ are the shear strain of the string, and $\psi_s(x,t)\,(s=z,y)$ are the rotation angle of the cross-section with respect to the $s-$axis. Furthermore, considering the linear stress–strain relationship, viscous damping, and external forces, the motion of "the speaking part of the spatial string" is expressed with five variables (three translations and two rotations) as follows:

Translation in the $z-$ and $y-$axes

$$\left\{c_0'\left(\frac{\partial^2}{\partial t^2}+b_{zy}'\frac{\partial}{\partial t}\right) - c_7'\frac{\partial^2}{\partial x^2}\right\}u_s(x,t) + c_6'\frac{\partial}{\partial x}\psi_s(x,t) + g_s^{nonl}(x,t)$$
$$= f_{Ha}(t)\,e_{Hs}\,\delta(x-x_H) - \sum_{i_D=1}^{I_D} f_{Ds}^{[i_D]}(t)\,\delta(x-x_D^{[i_D]}) \qquad s=z,y \tag{6a}$$

$$\text{with}\quad g_s^{nonl}(x,t) = -c_3'\frac{\partial}{\partial x}\left[\frac{\partial}{\partial x}\,u_s\Big[1-\left\{\left(1+\frac{\partial}{\partial x}u_x\right)^2+\left(\frac{\partial}{\partial x}u_y\right)^2+\left(\frac{\partial}{\partial x}u_z\right)^2\right\}^{-\frac{1}{2}}\Big]\right]$$

Rotation in the $zx-$ and $yx-$planes

$$c_6'\frac{\partial}{\partial x}u_s(x,t) + \left\{-c_5'\left(\frac{\partial^2}{\partial t^2}+b_{zy}'\frac{\partial}{\partial t}\right) - c_6' + c_4'\frac{\partial^2}{\partial x^2}\right\}\psi_s(x,t) = 0 \qquad s=z,y \tag{6b}$$

Translation in the $x-$axis

$$\left\{c_0'\left(\frac{\partial^2}{\partial t^2}+b_x'\frac{\partial}{\partial t}\right) - c_2'\frac{\partial^2}{\partial x^2}\right\}u_x(x,t) + g_x^{nonl}(x,t)$$
$$= f_{Ha}(t)\,e_{Hx}\,\delta(x-x_H) - \sum_{i_D=1}^{I_D} f_{Dx}^{[i_D]}(t)\,\delta(x-x_D^{[i_D]}) \tag{6c}$$

$$\text{with} \quad g_x^{nonl}(x,t) = c'_3 \frac{\partial}{\partial x}\left[\left(1+\frac{\partial}{\partial x}u_x\right)\left\{\left(1+\frac{\partial}{\partial x}u_x\right)^2+\left(\frac{\partial}{\partial x}u_y\right)^2+\left(\frac{\partial}{\partial x}u_z\right)^2\right\}^{-\frac{1}{2}}\right]$$

where $g_s^{nonl}(x,t)\,(s=z,x,y)$ are the terms caused by the geometrical nonlinearity. In pianos, wrapped strings are used for the low range, whereas plain strings are used for the mid–high range. The former consists of the core and copper wires, and the latter consists of only the core wire. $c'_0\,(=\rho_f S$ for plain strings) is the linear density, $c'_1\,(=ES\varepsilon_0)$ the tension, $c'_2\,(=ES)$ the extensional rigidity, $c'_3=c'_2(1-\varepsilon_0)$. $c'_4\,(=EI)$ is the flexural rigidity, $c'_5\,(=\rho_f I$ for plain strings) the rotational inertia, and $c'_6\,(=kGS)$ the shear rigidity. $c'_7=c'_1+c'_6$. $\rho_f$ is the density of the core wire, $E$ and $G$ are the moduli of the longitudinal and transverse elasticity of the core wire, respectively, and $k$ is the nondimensional Timoshenko shear coefficient. $b'_{zy}$ and $b'_x$ are the transverse and longitudinal mass proportional viscous damping coefficients of the string, respectively, $S\,(=\pi(d_f)^2/4)$ the cross-sectional area, $I\,(=\pi(d_f)^4/64)$ the second moment of area, and $d_f$ the diameter of the core wire. For the wrapped strings, by approximating the helical structure of the copper wire with multiple donut-shaped structures, $c'_0$ and $c'_5$ are calculated using $\rho_f$, $\rho_c$, $d_f$, and $d_c$, where $\rho_c$ and $d_c$ are the density and diameter of the copper wire, respectively. Here, the small increase in stiffness due to the core wire is neglected. $f_{Ds}^{[i_D]}(t)\,(s=z,x,y)$ are the forces exerted by the damper on the string, $x_D^{[i_D]}$ are the damping points, $i_D$ and $I_D$ are the index and number of the damper tip in contact with the certain string, respectively, and $\delta$ is the Dirac delta function. The equations of motion of "the rear duplex part of the spatial string" are expressed by removing the nonlinear terms $g_s^{nonl}(x,t)\,(s=z,x,y)$ and the external force terms $f_{Ha}(t)$, $f_{Ds}^{[i_D]}(t)\,(s=z,x,y)$ from Eq. (6).

Fig. 4 shows an image of a bridge, which is one of the string support parts. Two bridge pins are embedded apart in the bridge in the direction of the string, forming an angle with the vertical plane in opposite directions. This string end-support condition is often referred to as the zig-zag end condition (see Chaigne et al. [11], Tan [12]). The boundary condition of the string modeled based on the beam theory must be defined on its translation and rotation. The translation of the string at its support ends is constrained by the bridge and the cast-iron frame, and the rotation of the string at its support ends can be considered to be somewhere between "constrained" and "unconstrained." Such intermediate conditions can be modeled using the rotational spring, as shown in Fig. 5. Considering the end of the bridge side, the string is constrained more firmly by the relatively stiffer metal bridge pin than by the relatively less stiff wooden bridge top. On the other hand, considering the end of the cast-iron frame side, the string is constrained more firmly in the normal direction than in the tangent direction to the cast-iron frame. In addition, the tilt of the bridge pin yields a clear anisotropy between the two support ends, as shown in Fig. 6.



**Fig. 4** Zig-zag end condition at the bridge.

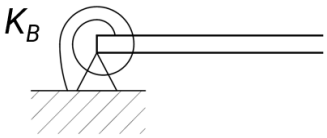



**Fig. 5** Rotational-spring support model at string ends. $K_B$ denotes the rotational spring constant.

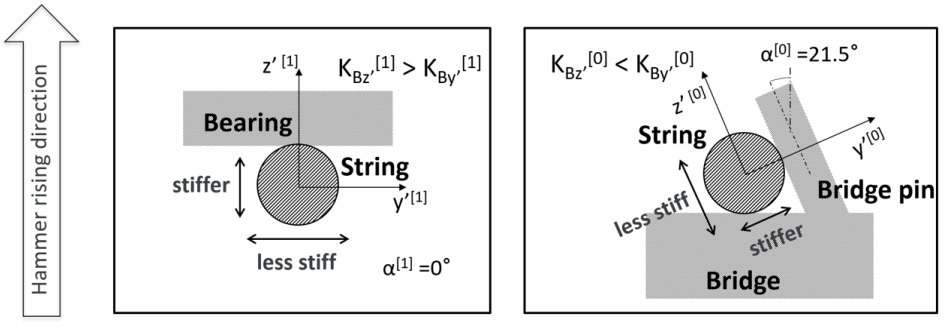



**Fig. 6** Cross-sectional view of anisotropic string end support.

Based on the above considerations, the boundary conditions of "the speaking part of the spatial string" are expressed as follows:

Translation in the $z-$, $x-$ and $y-$axes

$$u_s(x,t) = u_{Bs}^{[i_B]}(t) \qquad x = (-1)^{i_B} l^{[1]};\ i_B = 0,\ 1;\ s = z, x, y \quad \text{(7a)}$$

Rotation in the $z'^{\,[i_B]}\,x-$plane

$$\begin{aligned} &\cos\alpha^{[i_B]}\left[c_4'\frac{\partial}{\partial x}\psi_z(x,t) + (-1)^{i_B} K_{Bz'}^{[i_B]}\left\{\psi_z(x,t) - \theta_{Bz}^{[i_B]}(t)\right\}\right] \\ &-\sin\alpha^{[i_B]}\left[c_4'\frac{\partial}{\partial x}\psi_y(x,t) + (-1)^{i_B} K_{Bz'}^{[i_B]}\left\{\psi_y(x,t) - \theta_{By}^{[i_B]}(t)\right\}\right] = 0 \\ &\qquad\qquad x = (-1)^{i_B} l^{[1]};\ i_B = 0,\ 1 \end{aligned} \quad \text{(7b)}$$

Rotation in the $y'^{\,[i_B]}\,x-$plane

$$\begin{aligned} &\sin\alpha^{[i_B]}\left[c_4'\frac{\partial}{\partial x}\psi_z(x,t) + (-1)^{i_B} K_{By'}^{[i_B]}\left\{\psi_z(x,t) - \theta_{Bz}^{[i_B]}(t)\right\}\right] \\ &+\cos\alpha^{[i_B]}\left[c_4'\frac{\partial}{\partial x}\psi_y(x,t) + (-1)^{i_B} K_{By'}^{[i_B]}\left\{\psi_y(x,t) - \theta_{By}^{[i_B]}(t)\right\}\right] = 0 \\ &\qquad\qquad x = (-1)^{i_B} l^{[1]};\ i_B = 0,\ 1 \end{aligned} \quad \text{(7c)}$$

where $u_{Bs}^{[i_B]}(t)\,(s = z, x, y)$ and $\theta_{Bs}^{[i_B]}(t)\,(s = z, y)$ are the translation displacement and rotation angles at the support ends, i.e., the portions of the body, respectively. $i_B = 0$ and $i_B = 1$ denote the bridge and cast-iron frame (bearing) sides of the speaking part of the string, respectively, and $\alpha^{[0]}$ and $\alpha^{[1]}$ denote the inclination angle of the bridge pin and the normal to the cast-iron frame with respect to the $zx-$plane, respectively. The $xy'z'^{\,[i_B]}$-coordinate system is defined as one rotated clockwise the $xyz-$ coordinate system around the $x$-axis by $\alpha^{[i_B]}$. $K_{Bz'}^{[i_B]}$ and $K_{By'}^{[i_B]}$ denote the rotational spring constants around the $y'^{\,[i_B]}$- and $z'^{\,[i_B]}$-axes, respectively. They depend on the flexural rigidity and bending angle of the core wire. $K_{Bz'}^{[0]}$ also depends on the cut depth of the bridge top. The boundary conditions of "the rear duplex part of the spatial string" are represented by replacing $l^{[1]}$ in Eq. (7) with $l^{[2]}$. Notably, the zig-zag end condition is naturally modeled by considering the tilt of the bridge pins at both the speaking and rear duplex parts of the string.

When the hybrid-interface CMS (using the component modes calculated under the condition that the strings are unconstrained by the hammers/dampers and constrained by the body–air system) is employed to represent the displacement of the string influenced by the motions of the hammer/damper and body–air system, the translation displacements and rotation angles of "the speaking part of the spatial string" are given as expressed below. This method is usually used with FEM; however, herein, it is used with the semi-analytic method, which makes it easy to observe

the relationship between physical parameters and solutions.

$$u_s(x,t) = \sum_{r_{zy}=1}^{R_{zy}} \xi_s^{[r_{zy}]}(t)\, U_s^{[r_{zy}]}(x) + \tilde{u}_s(x,t) \qquad s = z, y \tag{8a}$$

$$\psi_s(x,t) = \sum_{r_{zy}=1}^{R_{zy}} \xi_s^{[r_{zy}]}(t)\, \Psi_s^{[r_{zy}]}(x) + \tilde{\psi}_s(x,t) \qquad s = z, y \tag{8b}$$

$$u_x(x,t) = \sum_{r_x=1}^{R_x} \xi_x^{[r_x]}(t)\, U_x^{[r_x]}(x) + \tilde{u}_x(x,t) \tag{8c}$$

where $U_s^{[r_{zy}]}(x)\,(s = z, y)$ and $U_x^{[r_x]}(x)$ are the hybrid-interface modes of the transverse and longitudinal translation of the string, respectively. $\Psi_s^{[r_{zy}]}(x)\,(s = z, y)$ are the hybrid-interface modes of the rotation angle of the string, $\xi_s^{[r_{zy}]}(t)\,(s = z, y)$ and $\xi_x^{[r_x]}(t)$ are the modal coordinates, $r_{zy}$ and $r_x$ are the indices of the natural mode, $R_{zy}$ and $R_x$ are the numbers of the considered mode, and $\tilde{u}_s(x,t)\,(s = z, x, y)$ and $\tilde{\psi}_s(x,\, t)\,(s = z, y)$ are the constrained (static deformation) modes of translation and rotation of the string, respectively.

The hybrid-interface modes (natural modes) are represented below by applying the variable separation method to the homogeneous equations, which removes the nonlinear, external force, and attenuation terms from Eq. (6).

$$\begin{aligned} U_s^{[r_{zy}]}(x) = {} & A_s^{[r_{zy}]} \cosh(\mu_{zy}^{[r_{zy}]} x) + B_s^{[r_{zy}]} \sinh(\mu_{zy}^{[r_{zy}]} x) \\ & + C_s^{[r_{zy}]} \cos(\nu_{zy}^{[r_{zy}]} x) + D_s^{[r_{zy}]} \sin(\nu_{zy}^{[r_{zy}]} x) \\ & r_{zy} = 1, 2, \cdots, R_{zy};\ s = z, y \end{aligned} \tag{9a}$$

$$\begin{aligned} \Psi_s^{[r_{zy}]}(x) = {} & A_s^{[r_{zy}]} \hat{\mu}_{zy}^{[r_{zy}]} \sinh(\mu_{zy}^{[r_{zy}]} x) + B_s^{[r_{zy}]} \hat{\mu}_{zy}^{[r_{zy}]} \cosh(\mu_{zy}^{[r_{zy}]} x) \\ & - C_s^{[r_{zy}]} \hat{\nu}_{zy}^{[r_{zy}]} \sin(\nu_{zy}^{[r_{zy}]} x) + D_s^{[r_{zy}]} \hat{\nu}_{zy}^{[r_{zy}]} \cos(\nu_{zy}^{[r_{zy}]} x) \\ & r_{zy} = 1, 2, \cdots, R_{zy};\ s = z, y \end{aligned} \tag{9b}$$

$$U_x^{[r_x]}(x) = C_x^{[r_x]} \cos(\nu_x^{[r_x]} x) + D_x^{[r_x]} \sin(\nu_x^{[r_x]} x) \qquad r_x = 1, 2, \cdots, R_x \tag{9c}$$

with

$$\mu_{zy}^{[r_{zy}]} = \left[\{(\alpha_{zy}^{[r_{zy}]})^2 + \beta_{zy}^{[r_{zy}]}\}^{\frac{1}{2}} + \alpha_{zy}^{[r_{zy}]}\right]^{\frac{1}{2}}, \quad \nu_{zy}^{[r_{zy}]} = \left[\{(\alpha_{zy}^{[r_{zy}]})^2 + \beta_{zy}^{[r_{zy}]}\}^{\frac{1}{2}} - \alpha_{zy}^{[r_{zy}]}\right]^{\frac{1}{2}}$$

$$\alpha_{zy}^{[r_{zy}]} = -\frac{1}{2}\left\{\frac{c_0'(\Omega_{zy}^{[r_{zy}]})^2}{c_7'} + \frac{c_5'(\Omega_{zy}^{[r_{zy}]})^2 - c_6'}{c_4'} + \frac{(c_6')^2}{c_4' c_7'}\right\}, \quad \beta_{zy}^{[r_{zy}]} = \frac{c_0'(\Omega_{zy}^{[r_{zy}]})^2\{c_6' - c_5'(\Omega_{zy}^{[r_{zy}]})^2\}}{c_4' c_7'}$$

$$\hat{\mu}_{zy}^{[r_{zy}]} = \frac{1}{c_6'}\left\{c_7'\mu_{zy}^{[r_{zy}]} + c_0'\frac{(\Omega_{zy}^{[r_{zy}]})^2}{\mu_{zy}^{[r_{zy}]}}\right\}, \quad \hat{\nu}_{zy}^{[r_{zy}]} = \frac{1}{c_6'}\left\{c_7'\nu_{zy}^{[r_{zy}]} - c_0'\frac{(\Omega_{zy}^{[r_{zy}]})^2}{\nu_{zy}^{[r_{zy}]}}\right\}$$
$$\nu_x^{[r_x]} = \Omega_x^{[r_x]}\big(c_2'/c_0'\big)^{-\frac{1}{2}}$$

where $\Omega_{zy}^{[r_{zy}]}$ and $\Omega_x^{[r_x]}$ are the natural angular frequencies of the transverse and longitudinal vibrations, respectively. When the fundamental natural angular frequency of the transverse vibration $\Omega_{zy}^{[1]}$ is given, $\varepsilon_0$ and $\Omega_{zy}^{[r_{zy}]}\,(r_{zy} = 2, 3, \cdots, R_{zy})$ are uniquely determined by numerically solving the characteristic equations, i.e., a system of transcendental equations, with $u_{Bs}^{[i_B]}(t)\,(i_B = 0, 1;\ s = z, y)$ and $\theta_{B_s}^{[i_B]}(t)\,(i_B = 0, 1;\ s = z, y)$ replaced by 0 in Eq. (7). In addition, $\Omega_x^{[r_x]}\,(= r_x\pi/(2l^{[1]})\big(c_2'/c_0'\big)^{\frac{1}{2}};\ r_x = 1, 2, \cdots, R_x)$ are determined under the condition that $u_{Bx}^{[i_B]}(t)\,(i_B = 0, 1)$ is replaced with 0 in Eq. (7a). Furthermore, when normalizing the modal mass to unity, $A_s^{[r_{zy}]}, B_s^{[r_{zy}]}, C_s^{[r_{zy}]}, D_s^{[r_{zy}]}\ (r_{zy} = 1, 2, \cdots, R_{zy};\ s = z, y)$, $C_x^{[r_x]}$, and $D_x^{[r_x]}\ (r_x = 1, 2, \cdots, R_x)$ are uniquely determined. Applying the computational method that Kondo [13] used to prove the orthogonality of natural modes, the modal mass and stiffness can be expressed as follows:

$$M_{zy}^{[r_{zy}]} = \int_{-l^{[1]}}^{l^{[1]}}\left[c_0'\left\{\big(U_z^{[r_{zy}]}\big)^2 + \big(U_y^{[r_{zy}]}\big)^2\right\} + c_5'\left\{\big(\Psi_z^{[r_{zy}]}\big)^2 + \big(\Psi_y^{[r_{zy}]}\big)^2\right\}\right]dx$$
$$r_{zy} = 1, 2, \cdots, R_{zy} \qquad \text{(10a)}$$

$$\begin{aligned}K_{zy}^{[r_{zy}]} = \int_{-l^{[1]}}^{l^{[1]}}\Bigg[ & c_1'\left\{\big(\frac{d}{dx}U_z^{[r_{zy}]}\big)^2 + \big(\frac{d}{dx}U_y^{[r_{zy}]}\big)^2\right\} + c_4'\left\{\big(\frac{d}{dx}\Psi_z^{[r_{zy}]}\big)^2 + \big(\frac{d}{dx}\Psi_y^{[r_{zy}]}\big)^2\right\} \\ & + c_6'\left\{\big(-\Psi_z^{[r_{zy}]} + \frac{d}{dx}U_z^{[r_{zy}]}\big)^2 + \big(-\Psi_y^{[r_{zy}]} + \frac{d}{dx}U_y^{[r_{zy}]}\big)^2\right\}\Bigg]dx \\ & + \sum_{i_B=0}^{1}\Big\{\,\big(K_{Bz'}^{[i_B]}\cos^2\alpha^{[i_B]} + K_{By'}^{[i_B]}\sin^2\alpha^{[i_B]}\big)\big(\Psi_z^{[r_{zy}]}\big)^2 \\ & \quad - 2\,\big(K_{Bz'}^{[i_B]} - K_{By'}^{[i_B]}\big)\cos\alpha^{[i_B]}\sin\alpha^{[i_B]}\,\Psi_z^{[r_{zy}]}\,\Psi_y^{[r_{zy}]} \\ & \quad + \big(K_{Bz'}^{[i_B]}\sin^2\alpha^{[i_B]} + K_{By'}^{[i_B]}\cos^2\alpha^{[i_B]}\big)\big(\Psi_y^{[r_{zy}]}\big)^2\,\Big\}\Big|_{x=(-1)^{i_B}l^{[1]}}\end{aligned}$$
$$r_{zy} = 1, 2, \cdots, R_{zy} \qquad \text{(10b)}$$

$$M_x^{[r_x]} = \int_{-l^{[1]}}^{l^{[1]}} c_0'\big(U_x^{[r_x]}\big)^2\,dx \qquad r_x = 1, 2, \cdots, R_x \qquad \text{(10c)}$$

$$K_x^{[r_x]} = \int_{-l^{[1]}}^{l^{[1]}} c_2'\big(\frac{d}{dx}U_x^{[r_x]}\big)^2\,dx \qquad r_x = 1, 2, \cdots, R_x \qquad \text{(10d)}$$

where $M_{zy}^{[r_{zy}]}$ and $K_{zy}^{[r_{zy}]}$ $(r_{zy} = 1, 2, \cdots, R_{zy})$ are the modal mass and stiffness of the transverse mode, and $M_x^{[r_x]}$ and $K_x^{[r_x]}$ $(r_x = 1, 2, \cdots, R_x)$ are the modal mass and stiffness of the longitudinal mode, respectively. Rayleigh quotient $\left(\Omega_{zy}^{[r_{zy}]}\right)^2 = K_{zy}^{[r_{zy}]}/M_{zy}^{[r_{zy}]} = K_{zy}^{[r_{zy}]}$, $\left(\Omega_x^{[r_x]}\right)^2 = K_x^{[r_x]}/M_x^{[r_x]} = K_x^{[r_x]}$ can be used for consistency checks. Eq. (9b) shows that two polarities of the transverse mode can be separated (i.e., separating $M_{zy}^{[r_{zy}]}$ into $M_z^{[r_z]}$ and $M_y^{[r_y]}$; separating $K_{zy}^{[r_{zy}]}$ into $K_z^{[r_z]}$ and $K_y^{[r_y]}$) only when $(K_{Bz'}^{[i_B]} - K_{By'}^{[i_B]}) \cos\alpha^{[i_B]} \sin\alpha^{[i_B]} = 0\,(i_B = 0, 1)$.

The constrained modes are represented by solving the homogeneous equations, removing the nonlinear, external force, and time derivative terms from Eq. (6), as follows:

$$\tilde{u}_s(x,\,t) = a_s(t) + b_s(t)\,x + c_s(t)\,\cosh(c_{14}c_{67}x) + d_s(t)\,\sinh(c_{14}c_{67}x) \qquad s = z, y \tag{11a}$$

$$\tilde{\psi}_s(x,\,t) = b_s(t) + c_s(t)\frac{c_{14}}{c_{67}}\,\sinh(c_{14}c_{67}x) + d_s(t)\frac{c_{14}}{c_{67}}\,\cosh(c_{14}c_{67}x) \qquad s = z, y \tag{11b}$$

$$\tilde{u}_x(x,\,t) = a_x(t) + b_x(t)\,x \tag{11c}$$

$$\text{with} \quad c_{14} = (c_1'/c_4')^{\frac{1}{2}},\; c_{67} = (c_6'/c_7')^{\frac{1}{2}}$$

If $u_{Bs}^{[i_B]}(t)\,(i_B = 0, 1;\, s = z, x, y)$ and $\theta_{Bs}^{[i_B]}(t)\,(i_B = 0, 1;\, s = z, y)$ are given (see Eq. (32)), $a_s(t)$, $b_s(t)$, $c_s(t)$, $d_s(t)$ $(s = z, y)$, $a_x(t)$, and $b_x(t)$ are uniquely determined under the boundary condition (Eq. (7)).

To integrate the nonlinear partial differential equations (Eq. (6)) with respect to variable x, the Galerkin method [14] is employed. This involves substituting Eq. (8) into Eqs. (6a) and (6c), multiplying both sides by $U_s^{[r_{zy}]}(x)\,(r_{zy} = 1, 2, \cdots, R_{zy};\, s = z, y)$ and $U_x^{[r_x]}(x)\,(r_x = 1, 2, \cdots, R_x)$, respectively, and integrating them from $x = -l^{[1]}$ to $x = l^{[1]}$ with respect to variable $x$, and the following simultaneous nonlinear ordinary differential equations are obtained.

$$\begin{aligned}
&\left\{\frac{d^2}{dt^2} + b_{zy}'\frac{d}{dt} + (\,\Omega_{zy}^{[r_{zy}]}\,)^2\right\}\xi_{zy}^{[r_{zy}]}(t) + \int_{-l^{[1]}}^{l^{[1]}} g_s^{nonl}(x,t)\,U_s^{[r_{zy}]}(x)\,dx \\
&+ c_0'\left(\frac{\partial^2}{\partial t^2} + b_{zy}'\frac{\partial}{\partial t}\right)\int_{-l^{[1]}}^{l^{[1]}} \tilde{u}_s(x,\,t)\,U_s^{[r_{zy}]}(x)\,dx \\
&= f_{Ha}(t)\,e_{Hs}\,U_s^{[r_{zy}]}(x_H) - \sum_{i_D=1}^{I_D} f_{Ds}^{[i_D]}(t)\,U_s^{[r_{zy}]}(x_D^{[i_D]}) \qquad r_{zy} = 1, 2, \cdots, R_{zy};\; s = z, y
\end{aligned} \tag{12a}$$

$$\Big\{ \frac{d^2}{dt^2} + b'_x \frac{d}{dt} + (\,\Omega_x^{[r_x]}\,)^2 \Big\} \xi_x^{[r_x]}(t) + \int_{-l^{[1]}}^{l^{[1]}} g_x^{nonl}(x,t)\, U_x^{[r_x]}(x)\, dx$$
$$+ c'_0 \Big( \frac{\partial^2}{\partial t^2} + b'_x \frac{\partial}{\partial t} \Big) \int_{-l^{[1]}}^{l^{[1]}} \tilde{u}_x(x,\,t)\, U_x^{[r_x]}(x)\, dx$$
$$= f_{Ha}(t)\, e_{Hx}\, U_x^{[r_x]}(x_H) - \sum_{i_D=1}^{I_D} f_{Dx}^{[i_D]}(t)\, U_x^{[r_x]}(x_D^{[i_D]}) \qquad r_x = 1, 2, \cdots, R_x \tag{12b}$$

To describe the frequency dependence of string losses in detail, $b'_{zy}$ and $b'_x$ are replaced by $b_{zy}^{'[r_{zy}]}\,(r_{zy} = 1, 2, \cdots, R_{zy})$ and $b_x^{'[r_x]}\,(r_x = 1, 2, \cdots, R_x)$, which are expressed as follows:

$$\begin{aligned}
b_{zy}^{'[r_{zy}]} &= 2\,\zeta_{zy}^{[r_{zy}]}\omega \simeq 2\,\zeta_{zy}^{[r_{zy}]}\Omega_{zy}^{[r_{zy}]} \\
\zeta_{zy}^{[r_{zy}]} &= \big\{ \alpha'\omega^{-1} + \nu'\omega^{-\frac{1}{2}} + \eta'_{zy}\omega^0 + \beta'\omega^{p'} \big\}/2 \\
&\simeq \big\{ \alpha'(\,\Omega_{zy}^{[r_{zy}]})^{-1} + \nu'(\,\Omega_{zy}^{[r_{zy}]})^{-\frac{1}{2}} + \eta'_{zy}(\,\Omega_{zy}^{[r_{zy}]})^0 + \beta'(\,\Omega_{zy}^{[r_{zy}]})^{p'} \big\}/2 \\
\alpha' &= 4\pi\rho_a\eta_a/c'_0, \quad \nu' = \alpha'(2/\eta_a)^{\frac{1}{2}} r_e \\
b_x^{'[r_x]} &= 2\,\zeta_x^{[r_x]}\omega \simeq 2\,\zeta_x^{[r_x]}\Omega_x^{[r_x]} \\
\zeta_x^{[r_x]} &= \big\{ \eta'_x\omega^0 + \beta'\omega^{p'} \big\}/2 \simeq \big\{ \eta'_x(\,\Omega_x^{[r_x]})^0 + \beta'(\,\Omega_x^{[r_x]})^{p'} \big\}/2
\end{aligned}$$

where $\omega$ is the angular frequency. $\zeta_{zy}^{[r_{zy}]}$ and $\zeta_x^{[r_x]}$ are the transverse and longitudinal modal damping ratio of the string, respectively, and $\eta'_{zy}$ and $\eta'_x$ are the transverse and longitudinal structural damping coefficients of the string, respectively. Notably, $\eta'_{zy}$ and $\eta'_x$ include not only the internal friction of the string but also the friction between the string and support part. $\eta'_{zy}$ depends on the tension of the string [15, 16]. $\alpha'$ and $\nu'$ are the coefficients related to the air resistance of the string [17]. $\beta'$ and $p'(\geqq 1)$ are the damping correction coefficient and the damping correction exponent of the string, which are introduced to compensate modal truncation errors in the body–air system. $r_e\,(= d_f/2$ for plain strings) is the effective radius of the string. $\rho_a$ and $\eta_a$ are the density and kinematic viscosity coefficient of air, respectively. Herein, we use an approximation in which the angular frequency is replaced by the natural angular frequency to apply the damping model originally defined in the frequency domain to the time domain. It is known that when the attenuation is small, the frequency response functions of each mode before and after approximation match well [18].

The force $f_{Bs}^{[i_B]}(t)\,(i_B = 0,\ 1;\ s = z, x, y)$ and the moment of force $m_{Bs}^{[i_B]}(t)\,(i_B = 0,\ 1;\ s = z, y)$ at the support ends are described using the translation displacement and rotation angle as follows:

$$f_{Bs}^{[i_B]}(t) = (-1)^{i_B} \Big\{ -c'_7 \frac{\partial}{\partial x} u_s(x,t) + c'_6\, \psi_s(x,t) - f_s^{nonl}(x,t) \Big\}$$
$$x = (-1)^{i_B} l^{[1]};\ i_B = 0,\ 1;\ s = z, y \tag{13a}$$

$$\text{with} \quad f_s^{nonl}(x,t) = c_3' \frac{\partial}{\partial x} u_s \Big[ 1 - \Big\{ \Big(1 + \frac{\partial}{\partial x} u_x\Big)^2 + \Big(\frac{\partial}{\partial x} u_y\Big)^2 + \Big(\frac{\partial}{\partial x} u_z\Big)^2 \Big\}^{-\frac{1}{2}} \Big]$$

$$m_{Bs}^{[i_B]}(t) = (-1)^{i_B} c_4' \frac{\partial}{\partial x} \psi_s(x,t) \qquad x = (-1)^{i_B} l^{[1]};\ i_B = 0,\ 1;\ s = z, y \tag{13b}$$

$$f_{Bx}^{[i_B]}(t) = (-1)^{i_B} \Big\{ -c_2' \frac{\partial}{\partial x} u_x(x,t) - f_x^{nonl}(x,t) \Big\} \qquad x = (-1)^{i_B} l^{[1]};\ i_B = 0,\ 1 \tag{13c}$$

$$\text{with} \quad f_x^{nonl}(x,t) = c_3' \Big[ 1 - \Big(1 + \frac{\partial}{\partial x} u_x\Big) \Big\{ \Big(1 + \frac{\partial}{\partial x} u_x\Big)^2 + \Big(\frac{\partial}{\partial x} u_y\Big)^2 + \Big(\frac{\partial}{\partial x} u_z\Big)^2 \Big\}^{-\frac{1}{2}} \Big]$$

Eqs. (8) to (13) are derived for the speaking part of the spatial string. The equations for the rear duplex part of the spatial string are derived similarly by removing the nonlinear and external force terms, and replacing $l^{[1]}$ with $l^{[2]}$.

## 2.3 Damper

In the initial state, piano strings are suppressed from vibrating by dampers. When a piano key is pressed, the corresponding damper gradually moves away from the corresponding string, and eventually the string is completely released from the resistance of the damper, preparing to be struck by the hammer. Furthermore, in a piano, the degree of contact between the damper and string can be changed not only by the depression amount of the key but also by the depression amount of the damper pedal, thereby controlling how the sound stops and the degree of string resonance. In this paper, the mechanism of the damper in such a piano is succinctly expressed using the following equation, which describes the relationship between the damper's resistance force and the displacement of the damping point on the string.

$$f_{Ds}^{[i_D]}(t) = b_{Ds} \{ 1 - e_D(t) \}^{p_D} \frac{d}{dt} u_s(x_D^{[i_D]}, t) \qquad i_D = 1, 2, \cdots, I_D;\ s = z, x, y \tag{14}$$

$$\begin{aligned}
\text{with} \qquad b_{Ds} &= K_D'' / \Omega_{zy}^{[r_{zy}]} && r_{zy} = 1, 2, \cdots, R_{zy};\ s = z, y \\
b_{Ds} &= K_D'' / \Omega_x^{[r_x]} && r_x = 1, 2, \cdots, R_x;\ s = x \\
x_D^{[i_D]} &= x_H + L_D (i_D - 0.5) / I_D \\
e_D(t) &= max(\, e_K(t),\, e_P(t)\,) \\
e_K(t) &= 0\text{: The key is not depressed at all.} \\
0 \leqq e_K(t) &\leqq 1\text{: The key is depressed in halfway.} \\
e_K(t) &= 1\text{: The key is depressed completely.} \\
e_P(t) &= 0\text{: The damper pedal is not depressed at all.} \\
0 \leqq e_P(t) &\leqq 1\text{: The damper pedal is depressed in halfway.} \\
e_P(t) &= 1\text{: The damper pedal is depressed completely.}
\end{aligned}$$

where $K_D''$ and $p_D$ and the loss elastic coefficient and the nonlinear exponent of the damper, respectively. $L_D$ is the damper length. $e_K(t)$ and $e_P(t)$ are the nondimensional depression amount of the key and damper pedal, respectively. This simple damper model means "a structural damping model with one end connected to a rigid

wall and the other end connected to a damping point on the string" and there is still room for improvement, such as the fact that mass and bowed string mechanism are not taken into account.

## 2.4 Wood as a 3D orthotropic complex elastic material

When a structure is allowed to freely vibrate in the air, the vibrations gradually attenuate over time and eventually stop. Such damping phenomena can be attributed to four factors: 1) air resistance, 2) internal friction of the material, 3) friction at the joints of each part and the support of the structure, and 4) transfer of energy to other vibration systems through the support. 2) and 3) are called structural damping. Structural damping is proportional to amplitude and independent of frequency and exhibits the same phase as velocity [19]. To describe this phenomenon, the complex stiffness constant $k^*$ instead of real stiffness constant $k$ is often used as follows:

$$k^* = k' + jk'' = k'\,(1 + j\eta\,)$$

where $j$ is an imaginary unit, $k'$ and $k''$ are the storage and loss stiffness constants, respectively, and $\eta\,(= k''/k')$ is the loss factor.

Wood is widely used for various parts of musical instruments, such as soundboards and rims. This is attributed to the lightweight and high stiffness of wood, which allows for fast wave propagation. Murase and Sawada [20] also stated that wood exhibits relatively low modal damping at low frequencies and high modal damping at high frequencies. In contrast, metals exhibit low modal damping at all frequencies, whereas plastics have high modal damping at all frequencies. This unique property of wood contributes to the gentle and pleasant sounds of wooden musical instruments. The property is attributed to the fact that when a wooden board vibrates transversely, the contribution of shear deformation increases for higher modes, and the structural damping associated with shear deformation is larger than that of elongation deformation. This property can be represented by modeling wood as a macroscopically homogeneous, 3D orthotropic, complex elastic material with the anatomical directions $(L, R, T)$ aligned to the elastic principal axes (Fig. 7).

The stress–strain relationship in wood can be expressed as follows:

$$\{\sigma\} = (\,[\,D'\,] + j[\,D''\,])\{\varepsilon\}$$

$$\{\sigma\} = \{\,\sigma_L,\, \sigma_R,\, \sigma_T,\, \tau_{LR},\, \tau_{RT},\, \tau_{TL}\}^T,\ \{\varepsilon\} = \{\,\varepsilon_L,\, \varepsilon_R,\, \varepsilon_T,\, \gamma_{LR},\, \gamma_{RT},\, \gamma_{TL}\}^T$$

$$[\,D'\,]^{-1} = \begin{bmatrix} 1/E'_L & -\nu_{RL}/E'_R & -\nu_{TL}/E'_T & 0 & 0 & 0 \\ -\nu_{LR}/E'_L & 1/E'_R & -\nu_{TR}/E'_T & 0 & 0 & 0 \\ -\nu_{LT}/E'_L & -\nu_{RT}/E'_R & 1/E'_T & 0 & 0 & 0 \\ 0 & 0 & 0 & 1/G'_{RT} & 0 & 0 \\ 0 & 0 & 0 & 0 & 1/G'_{TL} & 0 \\ 0 & 0 & 0 & 0 & 0 & 1/G'_{LR} \end{bmatrix}$$

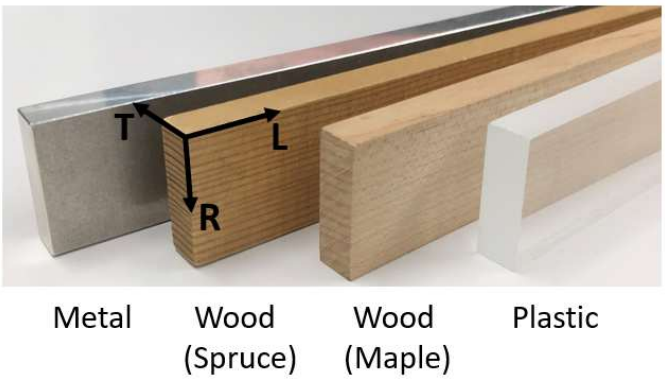



**Fig. 7** Three-dimensional orthotropic material directions of wood and associated elastic constants.

$$\text{with} \qquad \nu_{RL}/E'_R = \nu_{LR}/E'_L, \quad \nu_{TL}/E'_T = \nu_{LT}/E'_L, \quad \nu_{TR}/E'_T = \nu_{RT}/E'_R$$

$$[\,D''\,]^{-1} = \begin{bmatrix} 1/E''_L & -\nu_{RL}/E''_R & -\nu_{TL}/E''_T & 0 & 0 & 0 \\ -\nu_{LR}/E''_L & 1/E''_R & -\nu_{TR}/E''_T & 0 & 0 & 0 \\ -\nu_{LT}/E''_L & -\nu_{RT}/E''_R & 1/E''_T & 0 & 0 & 0 \\ 0 & 0 & 0 & 1/G''_{RT} & 0 & 0 \\ 0 & 0 & 0 & 0 & 1/G''_{TL} & 0 \\ 0 & 0 & 0 & 0 & 0 & 1/G''_{LR} \end{bmatrix}$$

where $\sigma$ and $\tau$ are the normal and shear stress, $\varepsilon$ and $\gamma$ the normal and shear strains, $[\,D'\,]$ and $[\,D''\,]$ the storage and loss elastic constant matrices, $E'$ and $E''$ the longitudinal storage and loss elastic moduli, $G'$ and $G''$ the transverse storage and loss elastic moduli, respectively. $\nu$ is Poisson's ratio. The loss factors are expressed as follows:

$$\eta_L = E''_L/E'_L, \quad \eta_R = E''_R/E'_R, \quad \eta_T = E''_T/E'_T,$$
$$\eta_{LR} = G''_{LR}/G'_{LR}, \quad \eta_{RT} = G''_{RT}/G'_{RT}, \quad \eta_{TL} = G''_{TL}/G'_{TL}$$

## 2.5 Manufacturing process

Without considering the nonlinearity involved in the manufacturing process, the equilibrium equation of the body can be described using FEM as follows:

$$[\,K'_b\,]\{u_b\} = \{f_b\} \tag{15}$$

where $\{u_b\} \in \mathbb{R}^{N_b}$ and $\{f\} \in \mathbb{R}^{N_b}$ are the displacement and external force vectors of the body, respectively. $N_b$ is the number of degrees of freedom (DOF) of the finite element model of the body. It becomes large when all the parts are assembled and the manufacturing of the body is completed. $[\,K'_b\,] \in \mathbb{R}^{N_b \times N_b}$ is the stiffness matrix

calculated based on the standard FEM theory as follows:

$$[\,K_b'\,] = \sum_m \int_V [\,B\,]^T [\,D'\,][\,B\,]\,dV \tag{16}$$

where the integral with $V$ denotes the integral in each element, and $\sum$ over m denotes a summation of all elements. $[B]$, which consists of derivatives of the shape functions of each element, satisfies the following equation:

$$\{\varepsilon\} = [\,B\,]\{u_b\}$$

The piano body manufacturing process involves the following steps:

(1) Gluing the bridge and ribs to the soundboard (manufacturing a soundboard assembly)

(2) Gluing the soundboard assembly to the rim

(3) Fastening a cast-iron frame to the soundboard–rim assembly with bolts (manufacturing a body)

(4) Stringing the body.

All the above-listed steps involve geometrical nonlinearity. In addition, steps (1)–(3) involve contact nonlinearity with slip during deformation.

Because of these processes, large manufacturing stress remains in the finished piano. Notably, the natural frequency and modal damping of a structure change depending on the residual stress. For example, the axial tensile stress in a beam transversely vibrating increases the natural frequency and decreases the modal damping, whereas the axial compressive stress decreases the natural frequency and increases modal damping [15, 16]. Therefore, to more accurately simulate piano sounds, the deformation and stress of the body must be calculated considering the geometrical and contact nonlinearity involved in successive manufacturing processes. This nonlinear static deformation analysis generally requires incremental solution schemes that divide the problem into steps for calculating the displacement and updating the stiffness. Therefore, the equilibrium equation can be expressed as follows:

$$[\,K_b'(\,u_b,\,f_b\,)\,]\{u_b\} = \{f_b\} \tag{17}$$

Here, $[B]$ in Eq. (16) is evaluated at the current deformed geometry in each step. Moreover, additional stiffness due to initial stresses is considered in each step [21].

## 2.6 Body

Notably, for the geometry and stiffness matrix of the body considered here, the effect of the manufacturing processes is already incorporated. The equations of motion of the body excited with a harmonic excitation angular frequency $\omega$ are derived using FEM as follows:

$$\begin{aligned} &(\,-\omega^2[M_b] + [K_b'] + j[K_b'']\,)\,\{U_b(\omega)\} = \{F_b\} \\ &\quad \text{with} \quad \{u_b(t)\} = \{U_b(\omega)\}\,e^{j\omega t},\ \{f_b(t)\} = \{F_b\}\,e^{j\omega t} \end{aligned} \tag{18}$$

where $\{u_b(t)\} \in \mathbb{C}^{N_b}$ and $\{U_b(\omega)\} \in \mathbb{C}^{N_b}$ are the displacement vector of the body and its complex amplitude vector, and $\{f_b(t)\} \in \mathbb{C}^{N_b}$ and $\{F_b\} \in \mathbb{R}^{N_b}$ are the external force vector and its complex amplitude vector, respectively. $[M_b] \in \mathbb{R}^{N_b \times N_b}$ is the mass matrix of the body, and $[K_b'] \in \mathbb{R}^{N_b \times N_b}$ is the structural damping matrix, which is expressed as follows:

$$[\,K_b''\,] = \sum_m \int_V [\,B\,]^T [\,D''\,][\,B\,]\,dV$$

By eliminating the attenuation term from the equation obtained by replacing $\omega$ and $\{F_b\}$ in (18) with $\Omega_b$ and $\{0\}$, respectively, the following real eigenvalue problem can be defined:

$$(\,-{\Omega_b}^2[M_b] + [K_b']\,)\{U_b(\Omega_b)\} = \{0\} \tag{19}$$

By solving this eigenvalue problem, the real eigenvalue ${\Omega_b}^2$ and the corresponding real eigenvector $\{\phi_b\} \in \mathbb{R}^{N_b}$ are obtained, where $\Omega_b$ denotes the undamped natural angular frequency of the body.

When the free-interface CMS (using the component modes calculated under the condition that the body is unconstrained by the strings and air) is employed to represent the displacement of a body influenced by the motion of the strings and air, the displacement amplitude of the body $\{U_b(\omega)\}$ can be expressed as follows:

$$\{U_b(\omega)\} = [\phi_b]\{q_b(\omega)\} \tag{20}$$

where $[\phi_b] \in \mathbb{R}^{N_b \times R_b}$ and $\{q_b(\omega)\} \in \mathbb{C}^{R_b}$ are the modal matrix (the matrix where the eigenvectors obtained above are arranged horizontally) and the modal coordinate, respectively, with the number of the considered natural mode $R_b$ ($<< N_b$). When Eq. (20) is substituted into Eq. (18) and multiplied by $[\phi_b]^T$ from the left side of Eq. (18), the following equation is obtained:

$$[\phi_b]^T(\,-\omega^2[M_b] + [K_b'] + j[K_b'']\,)\,[\phi_b]\,\{q(\omega)\} = [\phi_b]^T\{F_b\}$$

When $[\phi_b]$ is normalized such that $[\phi_b]^T[M_b][\phi_b] = [I_b]$, the following equation is obtained:

$$(-\omega^2[I_b] + [{\Omega_b}^2] + j[G_b]\,)\,\{q_b(\omega)\} = [\phi_b]^T\{F_b\} \tag{21}$$

$$\text{with} \quad [G_b] = [\phi_b]^T[K_b''][\phi_b] \tag{22}$$

where $[I_b] \in \mathbb{R}^{R_b \times R_b}$ is the identity matrix, and $[G_b] \in \mathbb{R}^{R_b \times R_b}$ is the symmetric modal structural damping matrix. $[{\Omega_b}^2] \in \mathbb{R}^{R_b \times R_b}$ is a diagonal matrix with $\left(\Omega_b^{[r_b]}\right)^2$ ($r_b = 1, 2, \ldots, R_b$) arranged diagonally, where $r_b$ denotes the index of the normal mode of the undamped body.

## 2.7 Body–air system

Here, we consider the problem of a coupled body–air system. We deal with external problems in which a body exists in an infinite domain or a semi-infinite domain, representing an anechoic chamber or a semi-anechoic chamber, respectively. In any case, the Sommerfeld condition is imposed as the boundary condition for infinity. To solve the 3D large-scale external acoustic problem of an object with complex shapes, either the FEM with PML or boundary element method (BEM) with the fast multipole method (FMM), i.e., FMBEM [22–24] is usually employed. In our preliminary trial on frequency response analysis of an external acoustic problem with the exact solution, i.e., a problem of acoustic radiation from a circular piston on a rigid sphere [25], the FMBEM outperformed the FEM with PML in terms of both accuracy and computational cost. Therefore, FMBEM is adopted here.

When the free-interface CMS (using the component modes calculated under the condition that the body–air system is unconstrained by the strings) is employed to represent the displacement of the body–air system influenced by the motion of the strings, the boundary integral equations based on the equations of motion of the coupled body–air system excited with the harmonic excitation angular frequency $\omega$ are derived using BEM with Eq. (21) as follows [26]:

$$\begin{bmatrix} [A_a(\omega)] & \omega^2 \rho_a \, [B_a(\omega)][C_a][\,\phi_a] \\ -(\,[C_a][\,\phi_a]\,)^T[S_a] & -\omega^2[I_b] + [\Omega_b{}^2] + j[G_b] \end{bmatrix} \begin{Bmatrix} P_a(\omega) \\ q_b(\omega) \end{Bmatrix} = \begin{Bmatrix} j\omega\rho_a \, [D_a(\omega)] \, \{Q_a\} \\ [\phi_b]^T \{F_b\} \end{Bmatrix} \tag{23}$$

$$\text{with} \quad \{p_a(t)\} = \{P_a(\omega)\} \, e^{j\omega t}, \;\; \{f_b(t)\} = \{F_b\} \, e^{j\omega t}$$

where $\{p_a(t)\} \in \mathbb{C}^{N_a}$ and $\{P_a(\omega)\} \in \mathbb{C}^{N_a}$ are the sound pressure vector on the surface of the body and its complex amplitude vector, respectively, and $N_a$ is the number of boundary elements on the surface of the body. $[\phi_a] \in \mathbb{R}^{3N_a \times R_b}$ is the modal matrix consisting of the $(X, Y, Z)$ component of the eigenvectors at the center of the boundary element, which is calculated by interpolating $[\phi_b]$. $[A_a(\omega)] \in \mathbb{C}^{N_a \times N_a}$ and $[B_a(\omega)] \in \mathbb{C}^{N_a \times N_a}$ are the influence coefficient matrices of the air on the body surface. $[C_a] \in \mathbb{R}^{N_a \times 3N_a}$ is the matrix comprising the direction cosine of the normal vector to the boundary element, $[S_a] \in \mathbb{R}^{N_a \times N_a}$ is a diagonal matrix comprising the boundary element area arranged diagonally, and $\{Q_a\} \in \mathbb{R}^{I_P}$ and $[D_a(\omega)] \in \mathbb{C}^{N_a \times I_P}$ are the volume velocity vector and the influence coefficient matrix at the point in the air with the number of the point source $I_P$. To overcome the difficulty of non-uniqueness in an external problem, $[A_a(\omega)]$, $[B_a(\omega)]$, and $[D_a(\omega)]$ are constructed using the Burton–Miller method. When the values of the right side of Eq. (23) are substituted, Eq. (23) becomes the system of linear equations with respect to the unknown variables $\{P_a(\omega)\}$ and $\{q_b(\omega)\}$. The solution to this problem, i.e., frequency response, can be obtained using an iterative method with FMM.

If the frequency response on the surface of a body surrounded by air can be expressed as a superposition of normal modes, then time-domain simulations of a coupled system consisting of nonlinear strings and a linear body–air system can be performed efficiently. The modal parameters on the surface of a body surrounded by air can be obtained by solving the following nonlinear eigenvalue problem, which is

defined by setting the right side of Eq. (23) as $\{0\}$ and replacing $\omega$ in the left side of Eq. (23) with the eigenvalue $\lambda$:

$$\begin{bmatrix} [A_a(\lambda)] & \lambda^2\rho_a\,[B_a(\lambda)][C_a][\,\phi_a] \\ -(\,[C_a][\,\phi_a]\,)^T[S_a] & -\lambda^2[I_b]+[\Omega_b{}^2]+j[G_b] \end{bmatrix} \begin{Bmatrix} P_a(\lambda) \\ q_b(\lambda) \end{Bmatrix} = \begin{Bmatrix} 0 \\ 0 \end{Bmatrix} \tag{24}$$

This nonlinear eigenvalue problem with dense, complex, and asymmetric matrix can be solved using the contour integral method with FMM [27–31]. By applying this method, the complex eigenvalues and right complex eigenvectors with the arbitrariness of constant multiples can be obtained. To completely determine the modal parameters on the body surface surrounded by air, it is necessary to determine not only the right but also the left eigenvectors and eliminate the arbitrariness of constant multiples, i.e., normalize the eigenvectors. To solve the remaining problems and enable time-domain simulations later, following the theory of experimental mode identification, we assume that the body surrounded by air can be approximated as a general viscous damping system (non-proportional viscous damping system) with a real symmetric matrix $[M]$, $[C]$ and $[K] \in \mathbb{R}^{N_b \times N_b}$, which includes the effect of structural damping and air resistance. Because our original body model is a structural damping system that includes an imaginary number, this assumption does not hold strictly. However, when dealing with a structural damping system in the time domain, it is necessary to approximate it with a viscous damping system. Here, the equations of motion of a piano body surrounded by air are described using its displacement vector $\{u_b(t)\} \in \mathbb{R}^{N_b}$ and external force vector $\{f_b(t)\} \in \mathbb{R}^{N_b}$ as follows:

$$[M]\{\ddot{u}_b(t)\} + [C]\{\dot{u}_b(t)\} + [K]\{u_b(t)\} = \{f_b(t)\} \tag{25}$$

These equations can be transformed as follows:

$$[D]\{\dot{w}_b(t)\} + [E]\{w_b(t)\} = \{g_b(t)\} \tag{26}$$

with

$$[D] = \begin{bmatrix} C & M \\ M & 0 \end{bmatrix}, \quad [E] = \begin{bmatrix} K & 0 \\ 0 & -M \end{bmatrix}, \quad \{w_b(t)\} = \begin{Bmatrix} u_b(t) \\ \dot{u}_b(t) \end{Bmatrix}, \quad \{g_b(t)\} = \begin{Bmatrix} f_b(t) \\ 0 \end{Bmatrix}$$

Substituting $\{w_b(t)\} = \{W_b(\lambda)\}e^{\lambda t}$ and $\{g_b(t)\} = \{0\}$ into Eq (26), the following complex eigenvalue problem can be defined.

$$(\lambda[D] + [E]\,)\,\{W_b(\lambda)\} = \{0\} \tag{27}$$

Considering that $[D]$ and $[E] \in \mathbb{R}^{2N_b \times 2N_b}$ are real symmetric matrices, if we solved this eigenvalue problem, the modal parameters (i.e., the complex eigenvalue $\lambda$ and the complex modal matrix $[\psi] \in \mathbb{C}^{N_b \times R}$ ) would be obtained with the number of the considered normal mode $R$. Using these modal parameters, the basic solution of Eq. (25) in the frequency domain, i.e., the frequency response function (compliance)

$H_b^{[i][l]}(\omega)$, is described as follows [32]:

$$H_b^{[i][l]}(\omega) = \frac{U_b^{[l]}(\omega)}{F_b^{[i]}} = \sum_{r=1}^{R}\left(\frac{Re^{[r][i][l]}}{j\omega - \lambda^{[r]}} + \frac{\bar{Re}^{[r][i][l]}}{j\omega - \bar{\lambda}^{[r]}}\right) \tag{28}$$

$$\text{with} \quad u_b^{[l]}(t) = U_b^{[l]}(\omega)\, e^{j\omega t},\ f_b^{[i]}(t) = F_b^{[i]}\, e^{j\omega t},\ \lambda^{[r]} = -\sigma^{[r]} + j\omega_d^{[r]},\ Re^{[r][i][l]} = \psi^{[r][i]}\psi^{[r][l]}$$

where $Re^{[r][i][l]}$ is the modal residue. $\sigma^{[r]}$ and $\omega_d^{[r]}$ are the modal decay rate and damped natural angular frequency, $\psi^{[r][i]}$ and $\psi^{[r][l]}$ are the components of the normalized complex eigenvector at points $i$ and $l$, and $r$, $i$ and $l$ are the indices of the normal mode, excitation and response points, respectively. The bar above a character indicates the conjugate of a complex number.

Notably, the aforementioned assumption holds that the modal parameters on the surface of the body obtained by Eq. (27) should be approximately equal to those obtained using Eq. (24). In addition, Eq. (28) derived from Eq. (27) indicates that the left and right eigenvectors are the same. Thus, normalized complex eigenvectors can be determined by solving the following linear least squares problem:

$$Minimize \quad \sum_{k,i,l}\left\{Er^{[k][i][l]}(z^{[r]})\right\}^2$$

$$Er^{[k][i][l]}(z^{[r]}) = \sum_{r=1}^{R}\left(\frac{Re^{[r][i][l]}}{j\omega^{[k]} - \lambda^{[r]}} + \frac{\bar{Re}^{[r][i][l]}}{j\omega^{[k]} - \bar{\lambda}^{[r]}}\right) - H_b^{[i][l]}(\omega^{[k]}) \tag{29}$$

$$\text{with} \quad \lambda^{[r]} = -\sigma^{[r]} + j\omega_d^{[r]},\ Re^{[r][i][l]} = \psi^{[r][i]}\psi^{[r][l]},\ \psi^{[r][i]} = z^{[r]}\psi_T^{[r][i]},\ \psi^{[r][l]} = z^{[r]}\psi_T^{[r][l]}$$

where $\lambda^{[r]}$, $\psi_T^{[r][i]}$, and $\psi_T^{[r][l]}$ are the eigenvalue and components of the non-normalized eigenvector at points $i$ and $l$, respectively. They are obtained by the nonlinear eigenvalue analysis of Eq. (24), considering Eq. (20). $H_b^{[i][l]}(\omega^{[k]})$ is the frequency response (compliance) obtained by the frequency response analysis of Eq. (23) with $\{Q_a\} = \{0\}$ and $F_b^{[i]} = 1$ at some representative points extracted from all the string support points, considering Eq. (20). $k$ is the index for discrete frequency, and $z^{[r]}$ is the complex decision variable. Notably, the matrices $[M]$, $[C]$, $[K]$, $[D]$ and $[E]$ in Eqs. (25)–(27) are only used for theoretical considerations and are not calculated in the proposed method.

When the complex CMS is applied to the coupled body–air system using the determined modal parameters, Eq. (28) yields the displacement expression using the complex modal coordinate $\eta^{[r]}(t)\,(r = 1, 2, \cdots, R)$ and linear ordinary differential equations with respect to the complex modal coordinate as follows:

$$u_b^{[l]}(t) = 2\sum_{r=1}^{R}\mathfrak{Re}\left[\,\psi^{[r][l]}\,\eta^{[r]}(t)\,\right] \tag{30}$$

$$\dot{\eta}^{[r]}(t) - \lambda^{[r]}\eta^{[r]}(t) = \sum_{i}\psi^{[r][i]}\,f_b^{[i]}(t) \qquad r = 1, 2, \cdots, R \tag{31}$$

Furthermore, when the displacement $u_b^{[l]}$ and external force $f_b^{[i]}(t)$ are replaced with the displacement of the string end-support $u_{Bs}^{[i_B]}(t)$ $(s = z, x, y)$ in Eq. (7) and the force exerted by the strings $f_{Bs}^{[i_B]}(t)$ $(s = z, x, y)$ in Eq. (13) respectively, Eqs. (30) and (31) yield the following equations:

$$u_{Bs}^{[i_K][i_W][i_L][i_B]}(t) = 2\sum_{r=1}^{R} \mathfrak{Re}\left[\, \hat{\psi}_{Bs}^{[r][i_K][i_W][i_L][i_B]}\, \eta^{[r]}(t) \,\right]$$

$$i_K = 1, 2, \cdots, I_K;\ i_W = 1, 2, \cdots, I_W^{[i_K]};\ i_L = 1,\ 2;\ i_B = 0,\ 1;\ s = z, x, y \quad (32)$$

$$\dot{\eta}^{[r]}(t) - \lambda^{[r]}\eta^{[r]}(t) = \sum_{i_K=1}^{I_K} \sum_{i_W=1}^{I_W^{[i_K]}} \sum_{i_L=1}^{2} \sum_{i_B=0}^{1} \sum_{s=z,x,y} \hat{\psi}_{Bs}^{[r][i_K][i_W][i_L][i_B]}\, f_{Bs}^{[i_K][i_W][i_L][i_B]}(t)$$

$$r = 1, 2, \cdots, R \quad (33)$$

$$\text{with} \qquad \hat{\psi}_{Bs}^{[r][i_K][i_W][i_L][i_B]} = \sum_{S=Z,X,Y} \beta_{Ss}^{[i_K][i_W][i_L][i_B]}\, \psi_{Bs}^{[r][i_K][i_W][i_L][i_B]}$$

where $i_K$ and $I_K$ $(= 88$ for general grand pianos) are the index and number of the key, respectively. $\beta_{Ss}^{[i_K][i_W][i_L][i_B]}$ are the direction cosine between the $XYZ-$ and $xyz-$cordinates, and $\psi_{Bs}^{[r][i_K][i_W][i_L][i_B]}$ are the components of the normal mode at the string support point on the $XYZ-$cordinate. The moment of force $m_{Bs}^{[i_K][i_W][i_L][i_B]}(t)$ in Eq. (13) can be approximately considered as a couple component of the force acting on two adjacent string support points. In the same way, the rotation angle $\theta_{Bs}^{[i_K][i_W][i_L][i_B]}(t)$ in Eq. (7) can be approximately considered as a rotation of the line defined by the two adjacent string support points.

## 2.8 Whole system

The equation of motion of the hammer Eq. (1), the equation of equilibrium of forces on the hammer felt Eq. (2), the equation of motion of each mode of the string (12), and the equation of motion of each mode of the body surrounded by air (33) are collectively referred to as the equation of motion of the whole system. Considering that the variables that represent the interactions between the substructures (i.e., $f_{Ha}^{[i_K][i_W]}(t)$, $f_{Hb}^{[i_K]}(t)$, $u_s^{[i_K][i_W]}(x_H^{[i_K][i_W]}, t)$, $f_{Bs}^{[i_K][i_W][i_L][i_B]}(t)$, $m_{Bs}^{[i_K][i_W][i_L][i_B]}(t)$, $u_{Bs}^{[i_K][i_W][i_L][i_B]}(t)$, and $\theta_{Bs}^{[i_K][i_W][i_L][i_B]}(t)$) are erasable intermediate variables, the equation of motion of the whole system can be expressed as simultaneous nonlinear ordinary differential equations with respect to the unknown variables $u_H^{[i_K]}(t)$, $u_{Hab}^{[i_K]}(t)$, $\xi_{zy}^{[r_{zy}][i_K][i_W][i_L]}(t)$, and $\xi_x^{[r_x][i_K][i_W][i_L]}(t)$ $(i_K = 1, 2, \cdots, I_K;\ i_W = 1, 2, \cdots, I_W^{[i_K]};\ i_L = 1, 2;$ $r_{zy} = 1, 2, \cdots, R_{zy}^{[i_K][i_L]};\ r_x = 1, 2, \cdots, R_x^{[i_K][i_L]})$; and $\eta^{[r]}(t)$ $(r = 1, 2, \cdots, R)$.

By setting the status of the piano at rest as the initial condition, the problem can be considered as the initial value problem of the simultaneous nonlinear ordinary differential equations. The motion of the whole system is created when the input to the system (the hammer's initial velocity) is given.

## 2.9 Sound radiation

The sound pressure at any observation point in the air $p^{[i_P]}(t)$ is calculated by a convolution operation as follows:

$$p^{[i_P]}(t) = \sum_{i_K=1}^{I_K} \sum_{i_W=1}^{I_W^{[i_K]}} \sum_{i_L=1}^{2} \sum_{i_B=0}^{1} \sum_{s=z,x,y} \int_0^t f_{Bs}^{[i_K][i_W][i_L][i_B]}(t-\tau)\, h_s^{[i_K][i_W][i_L][i_B][i_P]}(\tau)\, d\tau \qquad i_P = 1, 2, \cdots, I_P \tag{34}$$

$$\text{with} \quad h_s^{[i_K][i_W][i_L][i_B][i_P]}(t) = \frac{1}{2\pi} \int_{-\infty}^{\infty} H_s^{[i_K][i_W][i_L][i_B][i_P]}(\omega)\, e^{j\omega t} d\omega$$

where $H_s^{[i_K][i_W][i_L][i_B][i_P]}(\omega)$ is the frequency response function between the force exerted by the string at the string support point and the sound pressure at the observation point in air (the virtual microphone point), and $i_P$ and $I_P$ are the index and number of the virtual microphone points, respectively. When calculating $H_s^{[i_K][i_W][i_L][i_B][i_P]}(\omega)$, considering that the string support points (with 3D direction) are usually much more than the virtual microphone points, it is effective to use the reciprocity principle for structural-acoustic coupling problems as follows:

$$H_s^{[i_K][i_W][i_L][i_B][i_P]}(\omega) = \frac{P^{[i_P]}(\omega)}{F_{Bs}^{[i_K][i_W][i_L][i_B]}} = \frac{j\omega U_{Bs}^{[i_K][i_W][i_L][i_B]}(\omega)}{Q_a^{[i_P]}} \tag{35}$$

$$\text{with} \quad u_{Bs}^{[i_K][i_W][i_L][i_B]}(t) = U_{Bs}^{[i_K][i_W][i_L][i_B]}(\omega)\, e^{j\omega t}, \;\; f_{Bs}^{[i_K][i_W][i_L][i_B]}(t) = F_{Bs}^{[i_K][i_W][i_L][i_B]}\, e^{j\omega t}$$

This principle states that the sound pressure at point A in the air exerted by the force vector at point B on the structural surface is equal to the velocity vector at point B on the structural surface exerted by the volume velocity at point A in the air. $H_s^{[i_K][i_W][i_L][i_B][i_P]}(\omega)$ are obtained by solving the system of equations (23) with $Q_a^{[i_P]} = 1$ and $\{F_b\} = \{0\}$ at each frequency, considering Eq. (20).

# 3 Numerical analysis

A 3D model of the Yamaha concert grand piano CFX (W = 1.60 m, H = 1.85 m, D = 2.75 m) with an open top lid was constructed (Fig. 8). Considering the calculation accuracy, a hexahedral mesh rather than a tetrahedral mesh was applied to most parts. On this piano, $I_K$ is 88, $I_W$ is 1 from the 1st key (note A1) to the 8th key (note E1), 2 from the 9th key (note F1) to the 13th key (note A2), and 3 from the 14th key (note A#2) to the 88th key (note C8). Wrapped strings are incorporated from the 1st key (note A1) to the 20th key (note E2), whereas plain strings are incorporated from the 21st key (note F2) to the 88th key (note C8).

## 3.1 Preprocesses

Processes preceding the time-domain simulation are referred to as preprocesses.

**Table 1** Physical properties of the hammer. ($I_{Hb} = 2$)

| Physical properties | | A1 | A5 | C8 | Units |
|---|---|---|---|---|---|
| Hammer mass | $M_H$ | 13.2 | 9.12 | 5.33 | g |
| Stiffness coefficient (upper) | $K_{Ha}$ | $5.37 \times 10^2$ | $2.83 \times 10^3$ | $5.10 \times 10^4$ | N/mm$^{p_{Ha}}$ |
| Nonlinear exponent (upper) | $p_{Ha}$ | 4.20 | 5.69 | 4.50 | |
| Relaxation time (upper) | $\tau_{Ha}$ | $1.0 \times 10^{-5}$ | $1.0 \times 10^{-5}$ | $1.0 \times 10^{-5}$ | s |
| Positive real number (upper) | $\beta_{Ha}$ | 0.80 | 0.80 | 0.80 | |
| Stiffness coefficient (lower) | $K_{Hb}$ | $8.02 \times 10^3$ | $8.52 \times 10^3$ | $7.86 \times 10^4$ | N/mm$^{p_{Hb}}$ |
| Nonlinear exponent (lower) | $p_{Hb}$ | 2.00 | 2.00 | 1.50 | |
| Relaxation time (lower) | $\tau_{Hb}^{[1]}$ | $1.0 \times 10^{-5}$ | $1.0 \times 10^{-5}$ | $1.0 \times 10^{-5}$ | s |
| Positive real number (lower) | $\beta_{Hb}^{[1]}$ | 0.50 | 0.50 | 0.50 | |
| Relaxation time (lower) | $\tau_{Hb}^{[2]}$ | $5.0 \times 10^{-6}$ | $5.0 \times 10^{-6}$ | $5.0 \times 10^{-6}$ | s |
| Positive real number (lower) | $\beta_{Hb}^{[2]}$ | 0.20 | 0.20 | 0.20 | |
| Relative striking position | $1/2 - x_H/L$ | 0.126 | 0.123 | 0.054 | |

The preprocesses for hammers and strings include identifying the nonlinear viscoelasticity properties of the hammer felt and eigenvalue analysis (calculation of the eigenvalues and eigenmodes) of the strings.

The properties of the double-layer nonlinear generalized Maxwell model for the hammer felt were identified using the differential evolution algorithm [33] so that the spectrum of the final synthesized sound would be as close as possible to a piano recording. This approach is analogous to how piano technicians bring the output closer to an ideal sound in their imagination. Table 1 lists the values of the physical properties used for the hammers.

The initial normal strain of the strings $\varepsilon_0$ and the natural angular frequencies of the transverse vibration of the strings $\Omega_{zy}^{[r_{zy}]}$ ($r_{zy} = 2, 3, \cdots, R_{zy}$) in Eqs. (9a) and (9b) are determined by numerically solving the system of transcendental equations with quadruple precision. $A_s^{[r_{zy}]}, B_s^{[r_{zy}]}, C_s^{[r_{zy}]}, D_s^{[r_{zy}]}$ ($r_{zy} = 1, 2, \cdots, R_{zy}$; $s = z, y$) in Eqs. (9a) and (9b) are determined by solving the simultaneous linear equations with $A_z^{[r_{zy}]} = 1$ and then normalizing the modal mass to unity. Tables 2 and 3 list the physical properties used for the strings and ends of the strings, respectively, and Table 5 lists the numerical parameters used for the strings. The attenuation properties $\eta'_{zy}$, $\eta'_x$, $\beta'$, $p'$ and the string-ends properties $K_{Bz'}^{[0]}$, $K_{By'}^{[0]}$, $K_{Bz'}^{[1]}$, $K_{By'}^{[1]}$ were chosen so that the synthesized sound would be as realistic as possible, considering that the rotation of the string at its support ends is somewhere between "constrained" and "unconstrained." Due to the anisotropy of the string end supports, pairs of close angular frequencies occur in the natural angular frequency sequence of bending vibration. In the future, by focusing on these frequency differences, it is expected that the string-ends properties $K_{Bz'}^{[0]}$, $K_{By'}^{[0]}$, $K_{Bz'}^{[1]}$, and $K_{By'}^{[1]}$ can be adjusted more precisely. The normal modes of the strings were considered up to approximately 10 kHz (for the low range), 12 kHz (for the mid-range), and 14 kHz (for the high range).

Table 4 lists the values of the physical properties used for the dampers.

**Table 2** Physical properties of the string.

| Physical properties | | A1 | A5 | C8 | Units |
|---|---|---|---|---|---|
| Density of core wire | $\rho_f$ | $7.86 \times 10^3$ | $7.86 \times 10^3$ | $7.86 \times 10^3$ | kg/m$^3$ |
| Density of copper wire | $\rho_c$ | $8.82 \times 10^3$ | | | kg/m$^3$ |
| Modulus of longitudinal elasticity | $E$ | 200 | 200 | 200 | GPa |
| Modulus of transverse elasticity | $G$ | 80 | 80 | 80 | GPa |
| Timoshenko shear coefficient | $k$ | 0.9 | 0.9 | 0.9 | |
| Transverse structural damping coefficient | $\eta'_{zy}$ | $1.0 \times 10^{-5}$ | $1.0 \times 10^{-5}$ | $1.0 \times 10^{-5}$ | |
| Longitudinal structural damping coefficient | $\eta'_x$ | $1.0 \times 10^{-3}$ | $5.0 \times 10^{-1}$ | $5.0 \times 10^{-1}$ | |
| Damping correction coefficient | $\beta'$ | $2.0 \times 10^{-10}$ | $2.0 \times 10^{-11}$ | $3.0 \times 10^{-11}$ | s$^{p'}$ |
| Damping correction exponent | $p'$ | 1.50 | 1.54 | 1.60 | |
| String length (speaking part) | $L^{[1]}$ | 2.018 | 0.405 | 0.052 | m |
| String length (rear duplex part) | $L^{[2]}$ | 0.162 | 0.097 | 0.037 | m |
| Diameter of core wire | $d_f$ | $1.5 \times 10^{-3}$ | $9.8 \times 10^{-4}$ | $8.0 \times 10^{-4}$ | m |
| Diameter of copper wire | $d_c$ | $1.7 \times 10^{-3}$ | | | m |
| Fundamental frequency | $\Omega^{[1]}_{zy}/(2\pi)$ | 27.53 | 442.0 | 4323 | Hz |

**Table 3** Physical properties of the string end support.

| Physical properties | | A1 | A5 | C8 | Units |
|---|---|---|---|---|---|
| Bridge pin angle (bridge) | $\alpha^{[0]}$ | 21.5 | 21.5 | 21.5 | deg |
| Rotational spring constant (bridge) | $K^{[0]}_{Bz'}$ | 40 | 40 | 20 | N·m |
| Rotational spring constant (bridge) | $K^{[0]}_{By'}$ | 80 | 80 | 40 | N·m |
| bridge pin angle (iron frame) | $\alpha^{[1]}$ | 0.0 | 0.0 | 0.0 | deg |
| rotational spring constant (iron frame) | $K^{[1]}_{Bz'}$ | 60 | 60 | 30 | N·m |
| Rotational spring constant (iron frame) | $K^{[1]}_{By'}$ | 30 | 30 | 10 | N·m |

**Table 4** Physical properties of the damper

| Physical properties | | A1 | A5 | C8 | Units |
|---|---|---|---|---|---|
| Number of damper tips on each string | $I_D$ | 6 | 6 | 0 | |
| Loss elastic coefficient | $K''_D$ | $2.42 \times 10^3$ | $2.42 \times 10^3$ | | kg/s$^2$ |
| Nonlinear exponent | $p_D$ | 2.0 | 2.0 | | |
| Damper length | $L_D$ | $8.85 \times 10^{-2}$ | $5.52 \times 10^{-2}$ | | m |

**Table 5** Numerical parameters for the string. ($I_K = 88$)

| Numerical parameters | | A1 | A5 | C8 |
|---|---|---|---|---|
| Index of key | $i_K$ | 1 | 49 | 88 |
| Number of strings in each key | $I_W$ | 1 | 3 | 3 |
| Number of natural modes (speaking part) | $R^{[1]}_{zy}$ | 410 | 46 | 6 |
| Number of natural modes (speaking part) | $R^{[1]}_x$ | 24 | 3 | 0 |
| Number of natural modes (rear duplex part) | $R^{[2]}_{zy}$ | 16 | 10 | 4 |
| Number of natural modes (rear duplex part) | $R^{[2]}_x$ | 0 | 0 | 0 |

**Table 6** Physical properties of wood materials used in the piano body.

| Physical properties | | Spruce | Maple | Beech | Units |
|---|---|---|---|---|---|
| Density | $\rho$ | $0.45 \times 10^3$ | $0.69 \times 10^3$ | $0.62 \times 10^3$ | kg/m$^3$ |
| Modulus of longitudinal elasticity | $E'_L$ | 13.8 | 15.6 | 12.3 | GPa |
| Modulus of longitudinal elasticity | $E'_R$ | 0.94 | 2.03 | 1.32 | GPa |
| Modulus of longitudinal elasticity | $E'_T$ | 0.51 | 0.77 | 0.59 | GPa |
| Modulus of transverse elasticity | $G'_{LR}$ | 0.85 | 1.71 | 0.98 | GPa |
| Modulus of transverse elasticity | $G'_{RT}$ | 0.07 | 0.50 | 0.20 | GPa |
| Modulus of transverse elasticity | $G'_{TL}$ | 0.78 | 1.25 | 0.64 | GPa |
| Poisson's ratio | $\nu_{LR}$ | 0.37 | 0.42 | 0.40 | |
| Poisson's ratio | $\nu_{RT}$ | 0.44 | 0.74 | 0.65 | |
| Poisson's ratio | $\nu_{TL}$ | $1.7 \times 10^{-2}$ | $3.4 \times 10^{-2}$ | $2.4 \times 10^{-2}$ | |
| Loss factor | $\eta_L$ | $0.64 \times 10^{-2}$ | $0.74 \times 10^{-2}$ | $1.00 \times 10^{-2}$ | |
| Loss factor | $\eta_R$ | $1.76 \times 10^{-2}$ | $2.08 \times 10^{-2}$ | $2.06 \times 10^{-2}$ | |
| Loss factor | $\eta_T$ | $1.76 \times 10^{-2}$ | $2.08 \times 10^{-2}$ | $2.06 \times 10^{-2}$ | |
| Loss factor | $\eta_{LR}$ | $1.62 \times 10^{-2}$ | $1.63 \times 10^{-2}$ | $1.96 \times 10^{-2}$ | |
| Loss factor | $\eta_{RT}$ | $4.14 \times 10^{-2}$ | $4.14 \times 10^{-2}$ | $3.90 \times 10^{-2}$ | |
| Loss factor | $\eta_{TL}$ | $1.79 \times 10^{-2}$ | $1.87 \times 10^{-2}$ | $2.28 \times 10^{-2}$ | |

The preprocesses for the coupled body–air system reduce the physical information about the large-scale linear coupled system into complex modal parameters at the string support points of the body–air system and the impulse response between the force at the string support points and the sound pressure at the virtual microphone points. The preprocesses for the coupled body–air system are described as follows:

1) 3D modeling and meshing of the body
2) Nonlinear static analysis of the body using FEM (manufacturing process simulation)
3) Real eigenvalue analysis of the body using FEM
4) Calculation of the modal damping matrix of the body
5) Nonlinear eigenvalue analysis of the coupled body–air system using FMBEM
6) Frequency response analysis of the coupled body–air system using FMBEM (calculation of frequency response between the force and displacement at the string support points)
7) Normal mode identification of the coupled body–air system (normalizing the eigenvectors at the string support points)
8) Frequency response analysis of the coupled body–air system with FMBEM (calculation of frequency response between the force at the string support points and the sound pressure at the virtual microphone points)

Preprocess 1 involves defining materials that constitute the body. Tables 6 and 7 list the physical properties of the woods and metals used for the piano body, respectively. Spruce is used for the soundboard, ribs, braces, and key bed, whereas maple and beech are used for the bridge, rim, pin block, and legs. Brass and stainless steel are used for the casters and bridge pins, respectively. For wood properties, the average values obtained from vibration tests on a number of specimens were used [34].

**Table 7** Physical properties of metal materials used in the piano body.

| Physical properties | | Cast-iron | Brass | Stainless steel | Units |
|---|---|---|---|---|---|
| Density | $\rho$ | $7.20 \times 10^3$ | $8.40 \times 10^3$ | $7.93 \times 10^3$ | kg/m$^3$ |
| Modulus of longitudinal elasticity | $E'$ | 131 | 103 | 197 | GPa |
| Modulus of transverse elasticity | $G'$ | 50.4 | 39.6 | 74.0 | GPa |
| Poisson's ratio | $\nu$ | 0.30 | 0.30 | 0.33 | |
| Loss factor | $\eta$ | $2.0 \times 10^{-3}$ | $1.0 \times 10^{-4}$ | $2.0 \times 10^{-4}$ | |

**Table 8** Numerical parameters of the finite-element body model.

| Numerical parameters | | |
|---|---|---|
| Degree of freedom | $N_b$ | $3.5 \times 10^7$ |
| Number of normal modes | $R_b$ | $1.9 \times 10^4$ |

**Table 9** Physical properties of air. (assumed air temperature = 15 °C)

| Physical properties | | | Units |
|---|---|---|---|
| Density | $\rho_a$ | 1.225 | kg/m$^3$ |
| Speed of sound | $c_a$ | 340 | m/s |
| Kinematic viscosity coefficient | $\eta_a$ | $1.5 \times 10^{-5}$ | m$^2$/s |

Preprocesses 2 and 3 (the nonlinear static and real eigenvalue analysis) described by Eqs. (17) and (19) are performed using MSC Nastran SOL400 and MSC Nastran SOL103, respectively. Preprocess 4, described by Eq. (22), is calculated using MSC Nastran DMAP (Direct Matrix Abstraction Program). Table 8 lists the numerical parameters used for the body. The normal modes of the body are considered up to 11 kHz.

For Preprocesses 5 (the nonlinear eigenvalue analysis described by Eq. (24)), 6, and 8 (frequency response analysis described by Eq. (23)), Yamaha's in-house program named SoNATA (Software of Numerical AcousTic Analysis) is employed. In these analyses, the entire frequency range was divided into two: low-frequency (0–5 kHz) and high-frequency (5–12 kHz) ranges. To reduce computational costs, we ignored the force exerted on the body surface by air in the high-frequency range. This means replacing the lower-left submatrix of the left-side matrix in Eqs. (23) and (24) with 0. With future enhancements to our computational resources, we will no longer require this compromise for high frequency ranges. Tables 9 and 10 list the physical properties and numerical parameters of the coupled body–air system, respectively.

**Table 10** Numerical parameters of the coupled body–air system.

| Numerical parameters | | Low-frequency range | High-frequency range |
|---|---|---|---|
| Degree of freedom | $N_a$ | $5.0 \times 10^5$ | $2.0 \times 10^6$ |
| Number of normal modes | $R_a$ | $1.4 \times 10^4$ | $1.3 \times 10^4$ |
| Number of virtual microphone points | $I_P$ | 2 | 2 |

## 3.2 Time-domain simulation

To solve the initial value problem of the simultaneous nonlinear ordinary differential equations derived in Section 2, the trapezoidal rule, which is an implicit differential scheme with second-order accuracy, is employed. To represent the unknown variables in simultaneous nonlinear ordinary differential equations as $\{u(t)\}$, this scheme converts $\{\ddot{u}(t)\}, \{\dot{u}(t)\}, \{u(t)\}$ on the continuous time to the numerical expression by $\{u[k+1]\}, \{u[k]\}, \{u[k-1]\}$ on the discrete-time as follows:

$$\begin{aligned}
&\{\ddot{u}(t)\} \to (\{u[k+1]\} - 2\{u[k]\} + \{u[k-1]\})/(\Delta t)^2 \\
&\{\dot{u}(t)\} \to (\{u[k+1]\} - \{u[k-1]\})/(2\Delta t) \\
&\{u(t)\} \to (\{u[k+1]\} + 2\{u[k]\} + \{u[k-1]\})/4 \qquad \text{with} \quad t = k\Delta t; k = 0, 1, \cdots
\end{aligned}$$

where $k$ is the index of time, and $\Delta t$ is the time step. Considering that the frequency accuracy is important in musical tones, this scheme is applied with prewarping to the natural angular frequency of the string and the body–air system as follows:

$$\Omega_{pw} = (2/\Delta t)\ \tan(\Omega_{org}\,\Delta t/2)$$

where $\Omega_{org}$ denotes $\Omega_{zy}^{[r_{zy}]}\,(r_{zy} = 1, 2, \cdots, R_{zy})$, $\Omega_x^{[r_x]}\,(r_x = 1, 2, \cdots, R_x)$ or $\Omega^{[r]}(= \{(\sigma^{[r]})^2 + (\omega_d^{[r]})^2\}^{\frac{1}{2}};\ r = 1, 2, \cdots, R)$. $\Omega_{pw}$ denotes the prewarped natural angular frequency used in the time-domain implementation.

The integrals in Eqs. (4) and (5) are calculated using the Gauss–Legendre quadrature rule. The initial value problem of the simultaneous nonlinear ordinary differential equations is converted to a problem to sequentially solve the simultaneous nonlinear algebraic equations with respect to $\{u[k+1]\}\,(k = 0, 1, \cdots)$ on the discrete-time. These simultaneous nonlinear algebraic equations are solved using the block Newton and Gauss–Seidel methods with $\Delta t$ =1/88,200$s$ ($\simeq 11.34\mu s$).

The convolution of Eq. (34) is conducted in the frequency domain using a fast convolution algorithm.

The developed programs for synthesizing the sound of a piano were named PARTITA (Programs for ART of InTerAction). This is because the essence of music art produced by a musical instrument lies in the interactions among every constructive part, and the programs calculate the interaction of the entire system.

# 4 Results

## 4.1 Preprocesses

Fig. 9 shows the contour plots of the signed von Mises stress obtained by the nonlinear static analysis considering large deformations and contacts that simulate the manufacturing process. The total tension of all strings during the stringing (approximately 190 kN) generated large stress especially in the cast-iron frame. At each process, it was checked that the shape of the soundboard crown reproduced that of an actual piano with sufficient accuracy. Fig. 10 shows the real normal modes obtained from the real eigenvalue analysis of the body. Approximately 19,000 real eigenvalues were extracted in the frequency range of 0–11 kHz. Fig. 11 shows the complex eigenmodes obtained from the nonlinear eigenvalue analysis of the coupled body–air system. Approximately 14,000 complex eigenvalues were extracted in the region on the complex plane in a frequency range of 0–5 kHz and the range of the modal decay rate divided by $2\pi$ between 0 $s^{-1}$ and 120 $s^{-1}$.

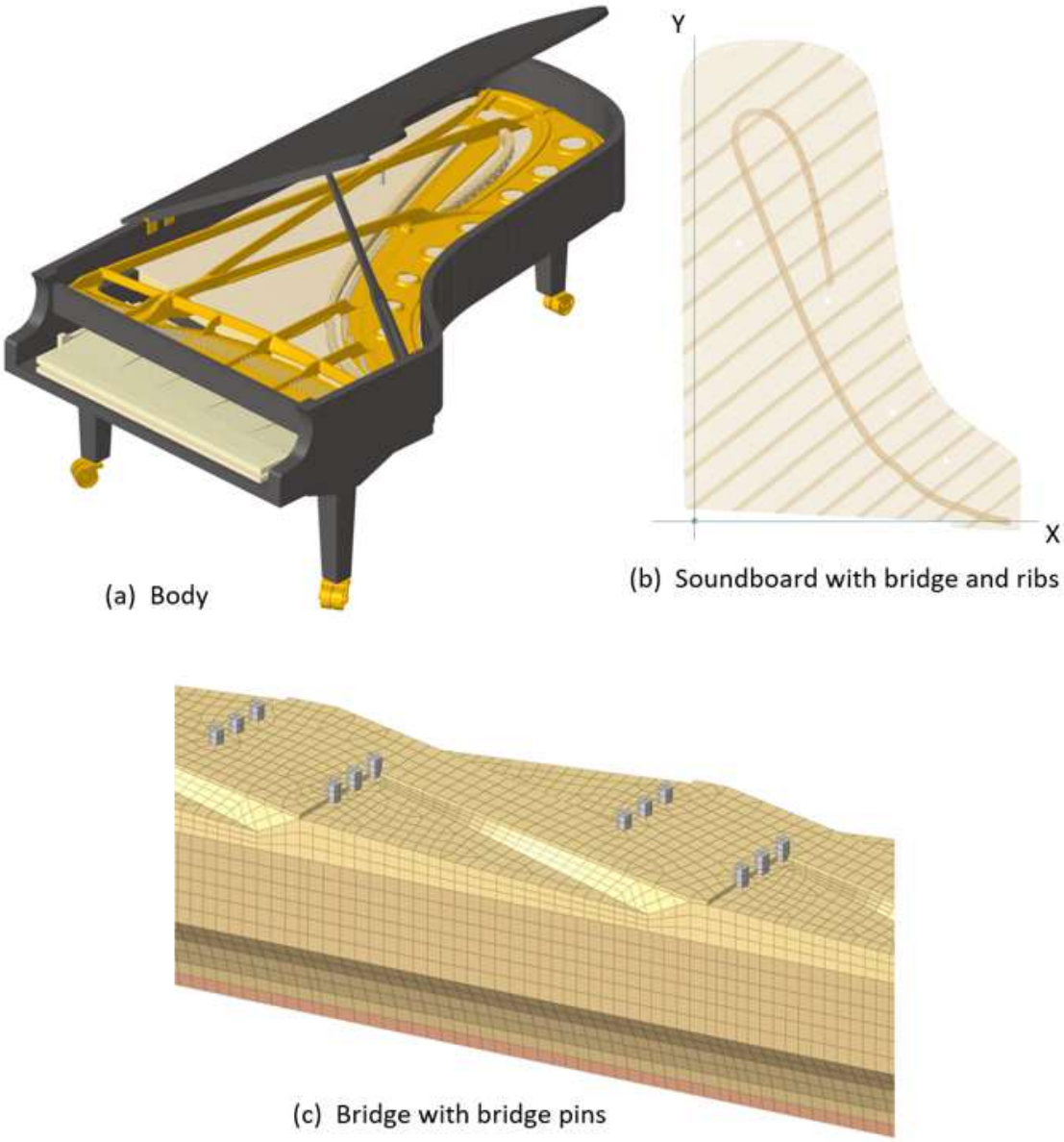



**Fig. 8** Three-dimensional finite-element model of the Yamaha concert grand piano CFX.

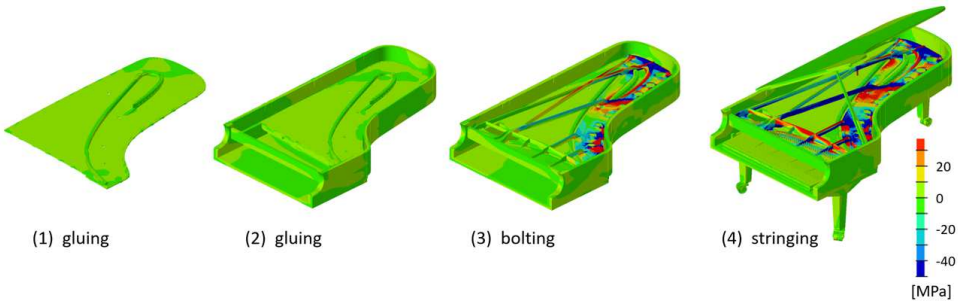



**Fig. 9** Residual stress distribution during successive manufacturing processes. The color scale indicates the signed von Mises stress. As expected, a large amount of stress was generated, especially in the cast-iron frame, during the stringing process.

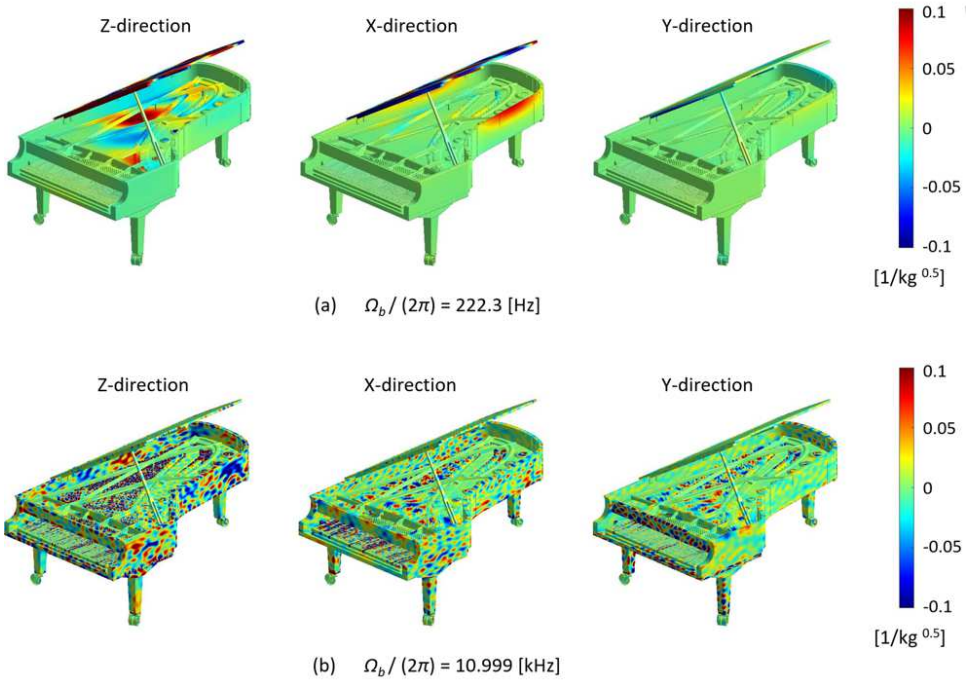



**Fig. 10** Representative real normal modes of the piano body obtained by real eigenvalue analysis. Approximately 19,000 real eigenvalues were extracted in the frequency range of 0–11 kHz.

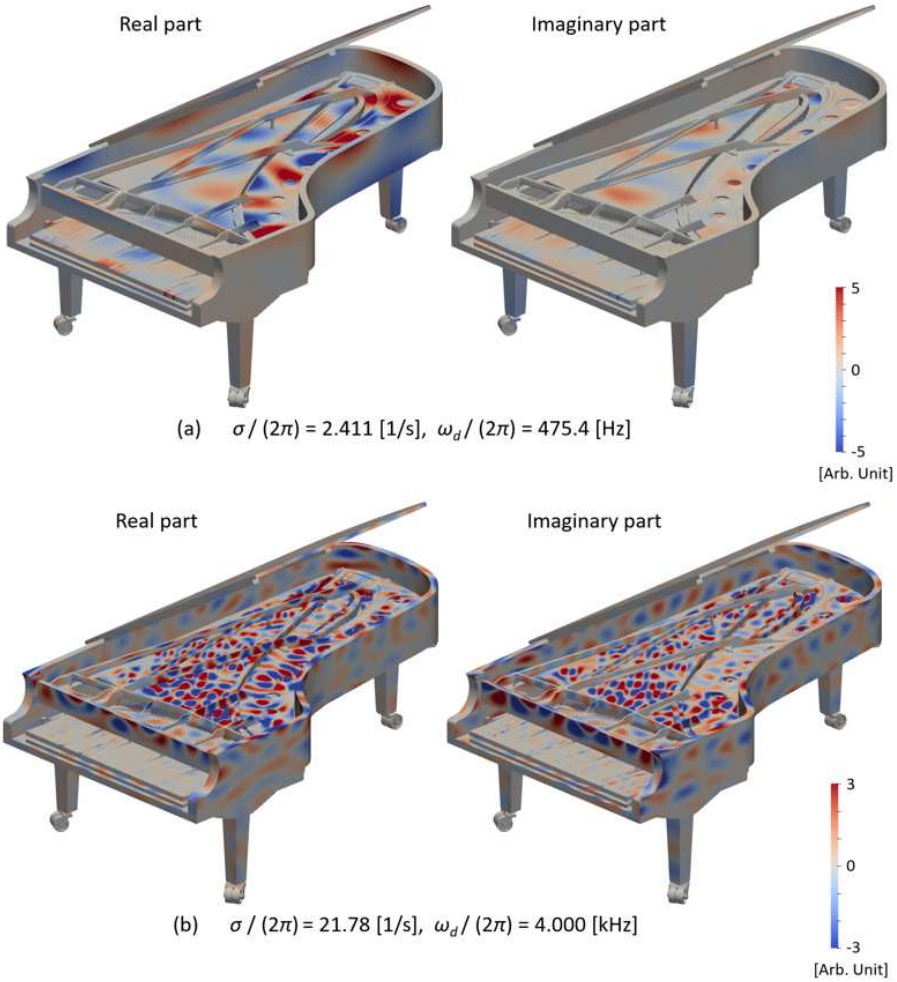



**Fig. 11** Representative complex eigenmodes of the coupled body–air system, illustrating normal surface displacement. Approximately 14,000 complex eigenvalues were extracted in the region on the complex plane in the frequency range of 0–5 kHz and the range of the modal decay rate divided by $2\pi$ between 0 $s^{-1}$ and 120 $s^{-1}$.

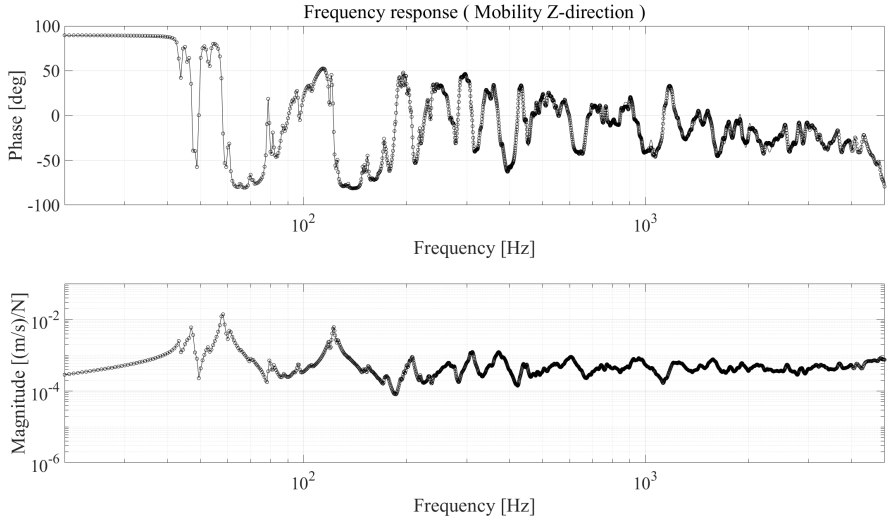



**Fig. 12** Driving-point mobility at a string support point on the bridge ($Z$-direction, note C#3). The solid line represents the directly computed frequency response, and the circles denote the response reconstructed by complex mode synthesis. The circles closely match the solid line.

Figs. 12–14 show the frequency response (driving-point mobility) of the velocity at a string support point when the force is applied at the same string support point. These figures correspond to the bridge in the $Z$-, $X$- and $Y$-directions of note C#3, respectively. The circles (the reconstructed frequency response from the mode synthesis shown by the first term on the right side of Eq. (29)) closely match the solid lines (the frequency response from the frequency response analysis shown by the second term on the right side of Eq. (29)). The curve fitting was satisfied simultaneously at all string support points in the three directions, which indicates that the frequency response was accurately reconstructed by superposing the complex normal modes.

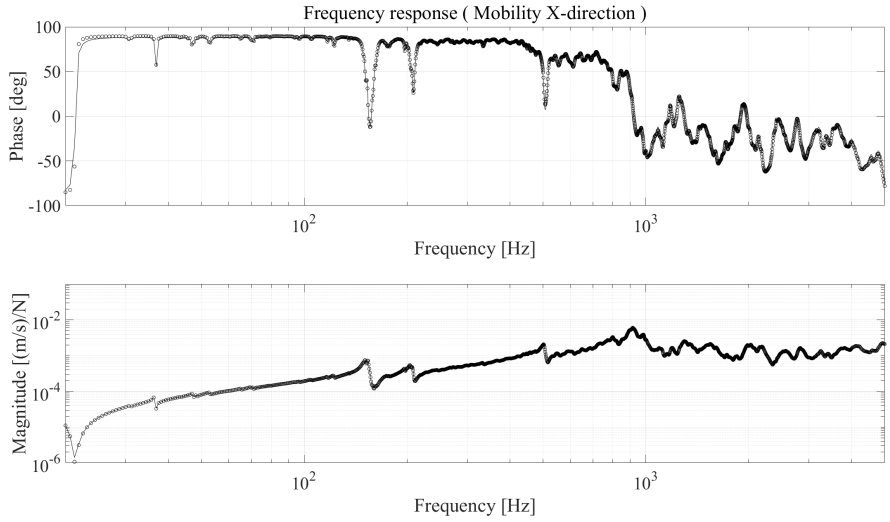



**Fig. 13** Driving-point mobility at a string support point on the bridge ($X$-direction, note C#3). The solid line represents the directly computed frequency response, and the circles denote the response reconstructed by complex mode synthesis. The circles closely match the solid line.

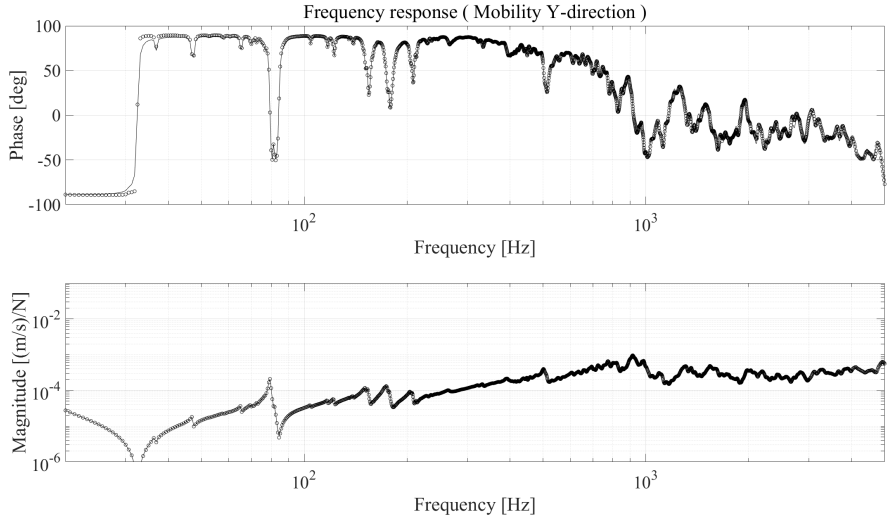



**Fig. 14** Driving-point mobility at a string support point on the bridge ($Y$-direction, note C#3). The solid line represents the directly computed frequency response, and the circles denote the response reconstructed by complex mode synthesis. The circles closely match the solid line.

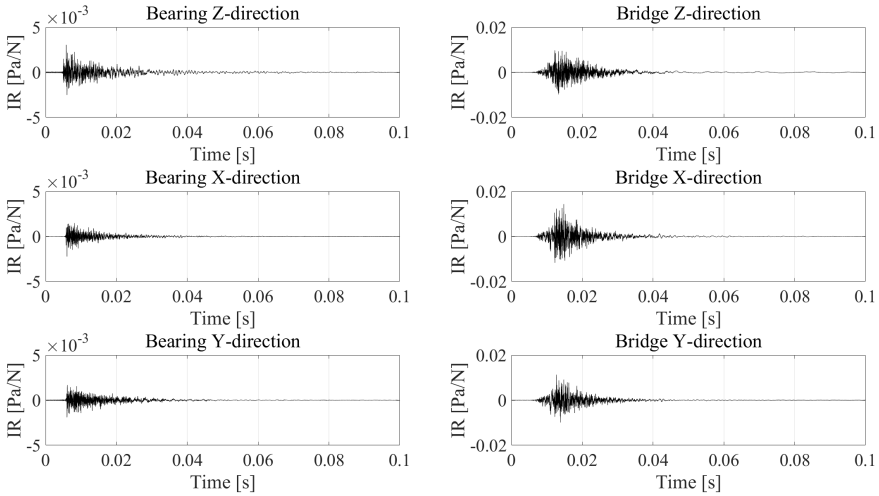



**Fig. 15** Impulse responses of sound pressure at a virtual microphone position due to three-dimensional forces applied at the string support points of note E1. Notably, the $Z$-, $X$-, and $Y$-directions refer to global coordinates relative to the body, not the local coordinates of each string.

Fig. 15 shows the impulse response (IR) of the sound pressure at a virtual microphone point when 3D forces are injected in the string support points of note E1. Although the IR of the bearing is smaller than that of the bridge, it should not be ignored when precise sound simulations are required. This figure also shows that the IR of the bearing increases faster than that of the bridge.

Thus, the dynamic characteristics of the large coupled body–air system are reduced to modal parameters (i.e., complex eigenvalues and complex normal modes at the string support points) and impulse response (from the string support points to the virtual microphone points).

## 4.2 Time-domain simulation

Before evaluating the results of the time-domain simulation, we confirmed that the numerical solution satisfies the energy theorem based on Newton's laws, which is a necessary condition to indicate that the numerical results were correct, i.e., there were no bugs in the programs.

Notably, herein, the 3D coupled problem between the hammer, the strings, and the body–air system was solved in the time domain. Fig. 16 shows the 3D force exerted by the struck string (the speaking part) at its support points, which is calculated using Eqs. (13a) and (13c). Because the string support point on the bearing is not far from the striking point, the first impulse waveform on the upper left side of Fig. 16 nearly shows the waveform of the force exerted by the hammer on the string. By contrast, because the string support point on the bridge is far from the striking point, the first impulse waveform on the upper right side of Fig. 16 shows the effect of dispersion of

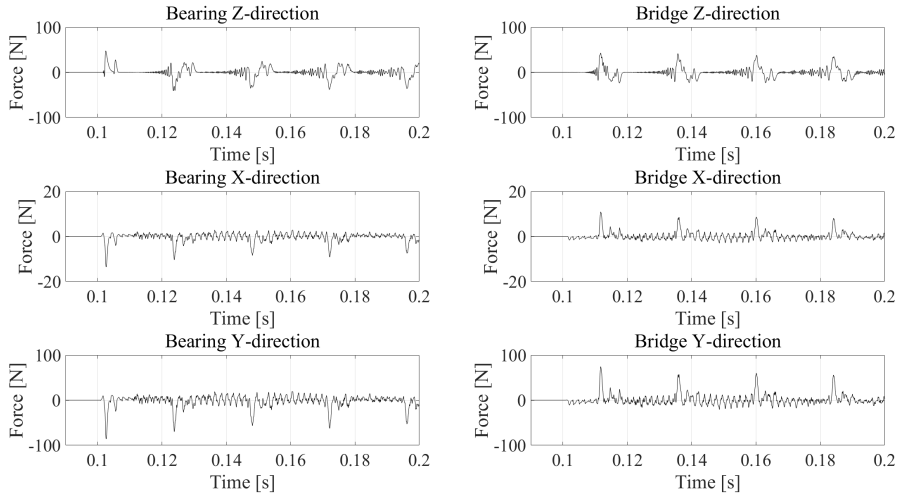



**Fig. 16** Time histories of forces exerted by the speaking string of note E1 at its support points following a hammer strike at 4 m/s. At $t = 0.1s$, the hammer tip is located 3 mm from the string at rest.

the transverse wave more clearly (Podlesak and Lee [35]). The forces on the bridge are transmitted faster in the $X$- and $Y$-directions than in the $Z$-direction because the propagation of the longitudinal wave of the string is faster than that of the transverse wave (see the right side of Fig. 16). Fig. 17 shows the sound pressure at two virtual microphone points. The sound pressure is synthesized by convolving the impulse response from each string support point to each virtual microphone point (shown in Fig. 15) with the force exerted by each string (shown in Fig. 16) and summing that at the ends of the speaking and rear duplex parts of all strings (Eq. (34)). The results in Figs. 16 and 17 were calculated under the condition that the string of note E1 was struck by the hammer at a speed of 4 m/s (a forte playing).

## 4.3 Piano Sound Synthesis

MIDI (Musical Instrument Digital Interface) data of various musical pieces recorded on a Yamaha Disklavier was used as input for the time-domain simulation, and the piano sounds at the pianist's listening position were synthesized. To demonstrate the reality of the simulated sounds and the usefulness of the auralization simulation, several audio samples are provided as supplementary materials (Online Resources 1–6).

First, we illustrate the effect of the dispersion of bending waves in the string and the geometrical nonlinearity of the string on the piano sound. The dispersion of bending waves in the string is caused by the string's bending stiffness (which is the main factor), rotational inertia, and shear deformation. Resources 1–4 are examples

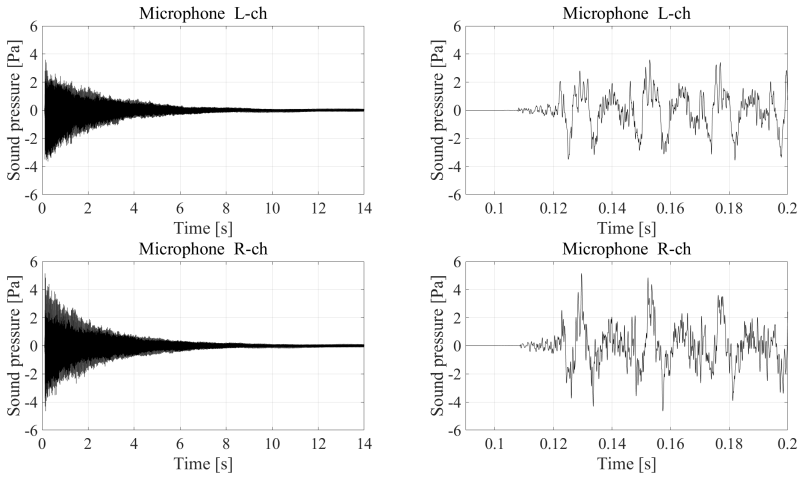



**Fig. 17** Synthesized sound pressure waveforms at two virtual microphone positions for note E1 struck at a hammer velocity of 4 m/s. At $t = 0.1s$, the hammer tip is located 3 mm from the string at rest.

of low range chromatic scale by a hard strike (hammer velocity of 5 m/s). Resource 1 is the recorded sound of Yamaha CFX and Resources 2–4 are the simulated sounds. Resource 2 is the case where both dispersion and geometrical nonlinearity are ignored. This case was calculated as $c_3' = c_4' = c_5' = c_6' = 0$ in Eq. (6). Resource 3 is the case where dispersion is taken into account and geometrical nonlinearity is ignored. This case was calculated as $c_3' = 0$ in Eq. (6). Resource 4 is the case where both dispersion and geometrical nonlinearity are taken into account. A comparative listening test among Resources 1–4 clarified that the importance of wave dispersion and geometrical nonlinearity in real piano sound. Resource 1 explains what happens if all partials' phase velocities of the string's bending wave are equal. The metallic ringing sound was clearly audible only in Resources 1 and 4.

The characteristics of the piano sound significantly depend on not only how the piano designer designs but also how the piano technician tunes. The next samples presented as Resource 5 and 6 clarify the effect of the deviation in unison tuning, i.e., the difference in pitch of multiple strings corresponding to one key, on the sound. These cases were calculated by changing $\varepsilon_0$ in Eq. (6). Resource 5 is a sound in which the pitches of multiple strings assigned to the same key are intentionally detuned from one another, within a range that is considered acceptable in practical piano tuning. Specifically, for a three-string unison, the pitch difference between the second string and the first string is set to 0.3 cents in the low range, 1.5 cents in the mid-range, and 2.5 cents in the high range, while the deviation of the third string is half of these values. Resource 6 is a reference sound in which all strings assigned to the same key are tuned to exactly the same pitch, representing an idealized, perfectly aligned condition used for comparison. Here, cent is a unit of pitch difference corresponding to 1/100 of a semitone; for a typical piano string, a deviation of 1 cent corresponds to only a few microns of string stretch. Consequently, this perfectly aligned condition represents an idealized reference that cannot be realized on an actual instrument.

The characters (a), (b) following Resource No. denote Scarlatti Sonata in E, Chopin Fantaisie-Impromptu, respectively. Resources 5 and 6 demonstrate that variations in unison tuning produce clearly perceptible changes in the resulting sound, although these differences are difficult to describe quantitatively using verbal descriptors alone.

Here, we emphasize the significance of auralization simulation for pianos. First, eliminating or controlling error factors can only be achieved through virtual experiments on a computer, i.e., simulation. When making an actual prototype, there are many error factors, such as material and manufacturing variations. These errors are inherent and cannot be eliminated. Second, by auralizing the simulation results, listeners can directly experience the causal relationship between specifications and the resulting sound with their own ears without the information missing by verbalization. Third, simulation allows us to explore parameter regimes inaccessible to physical prototyping. Resources 2, 3 and 6 are exactly such cases. In other words, simulation is not a simple substitute for the real thing.

In our time-domain simulation, it took about 1,200 seconds to synthesize one sound per second using 88 cores of a CPU (Intel Xeon Platinum 8592). For now, PARTITA still has a lot of room for improvement in parallelization efficiency.

# 5 Discussion

The primary objective of this work is not parameter identification accuracy, but the demonstration of a causal, integrable simulation framework. The presented framework numerically reproduces hallmark phenomena of piano sound production within a single, causally consistent simulation loop that spans hammer felt, spatial strings, and a 3D body–air system. In particular, the model captures the experimentally reported exchange of energy between the two transverse string polarizations (often termed "double polarization") and the emergence of metallic, non harmonic "ringing." Figs. 18–21 show that the simulated three-dimensional displacement and trajectories at the striking point evolve from predominantly vertical to increasingly horizontal motion, with elliptical loops and rotation direction changes comparable to reported measurements [36], thereby supporting the physical fidelity of the formulation. The key point is that it precisely expresses the three-dimensional connection between the strings and the body. By explicitly modeling the zig-zag end condition (inclined bridge pins) together with rotational spring support and distinct normal/tangential stiffnesses at both supports, the simulation naturally reproduces cross polarization coupling without resorting to ad hoc terms. The bidirectional coupling between longitudinal and transverse motion—retained to satisfy energy conservation—further explains amplitude dependent spectral enrichment and conditions under which partial sums lock to longitudinal resonances, contributing to audible ringing.

On the hammer side, a double layer nonlinear generalized Maxwell model was introduced to account for disparate viscoelastic behaviors of the tip and core. While Section 2 identified parameters via differential evolution based on the sound, we note that direct validation against measured force–compression loops and time resolved hammer–string force would further strengthen the claim of wide range fidelity. Such comparisons will quantify hysteresis, rate dependence, and the transition between soft and strong strikes across keys.

Regarding the body–air subsystem, the complex mode CMS based on nonlinear eigenvalue analysis reconstructs driving point mobilities (Figs. 12–14) with high accuracy across three spatial directions at the supports, demonstrating that dense exterior vibroacoustics can be reduced to a compact set of complex eigenvalues and residues suitable for time-domain use. In our current implementation, to contain cost we neglect air to structure feedback above 5kHz. This approximation is justified by the relatively small added mass and radiation induced stiffness corrections at high frequency compared with internal losses and by the fact that auralization in this range is dominated by structure to air radiation already captured by the identified modes. As computational resources improve, we plan to remove this high frequency simplification.

From an engineering science perspective, two aspects are broadly transferable. First, the manufacturing aware modeling: residual stresses introduced by gluing, bolting, and stringing measurably shift natural frequencies and modal damping. Embedding nonlinear static assembly analysis into the acoustic pipeline enables causal, design for sound studies not only for pianos but for other large wooden or composite structures where anisotropy and residual stress are significant. Second, the CMS centric reduction: combining hybrid interface CMS for nonlinear substructures

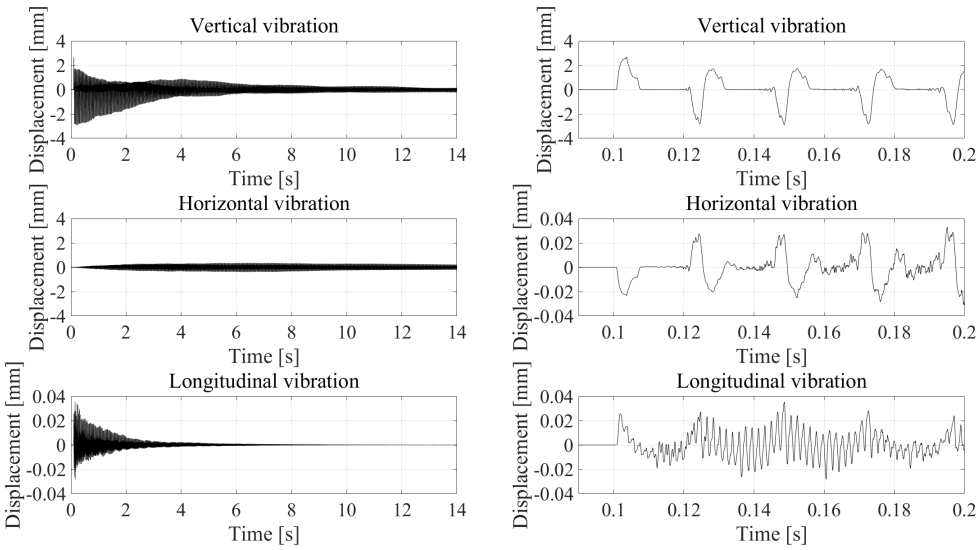



**Fig. 18** Three-dimensional displacement of the string at the striking point of note E1 following a hammer impact at 4 m/s. At $t = 0.1s$, the hammer tip is located 3 mm from the string at rest. The vertical, horizontal, and longitudinal vibrations correspond to $z$, inverted $y$, and $x$-directions in the local coordinates of the string, respectively.

with complex mode synthesis for exterior vibroacoustics provides a scalable route to parameter sensitive, time-domain simulations without sacrificing key perceptual cues.

Limitations suggest clear opportunities. We exclude action mechanism dynamics and damper behavior from the time-domain loop; incorporating these will refine onset/decay envelopes and pedaling effects. Finally, while we provided aural examples distinguishing dispersion and geometric nonlinearity and illustrating unison detuning, a systematic perceptual study (e.g., MUSHRA) would quantify thresholds and design sensitivities.

Overall, the results indicate that auralization driven engineering—tight coupling of high fidelity modeling, manufacturing realism, and perceptual evaluation—can make specification level choices (e.g., scale design, wood properties, crown geometry) and technician level adjustments (e.g., unison tuning) audibly and reproducibly traceable. We anticipate the method will accelerate evidence based piano design and inform scalable, physics based sound synthesis in other complex vibroacoustic systems.

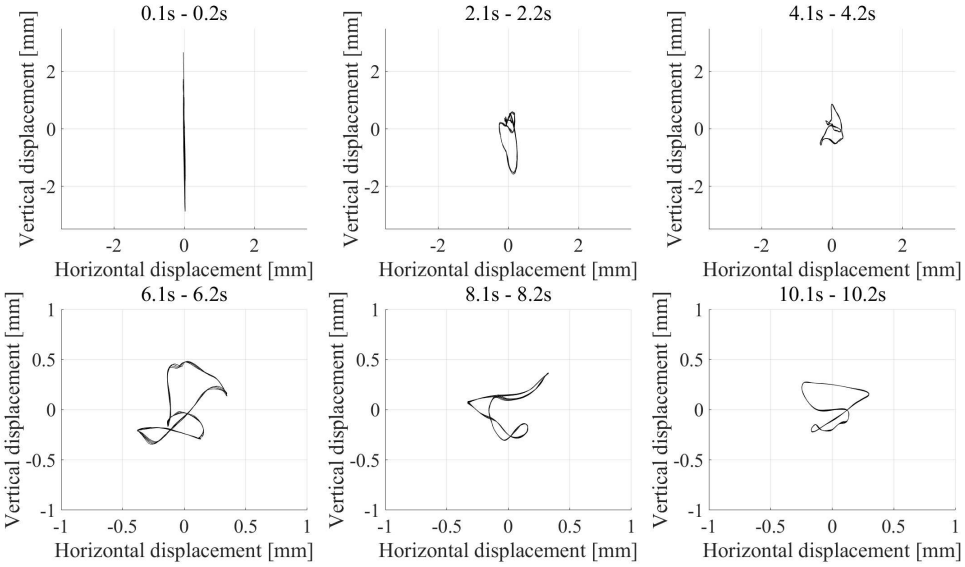



**Fig. 19** Trajectories consisting of the components in the $z$-direction and inverted $y$-direction of the displacement shown in Fig. 18

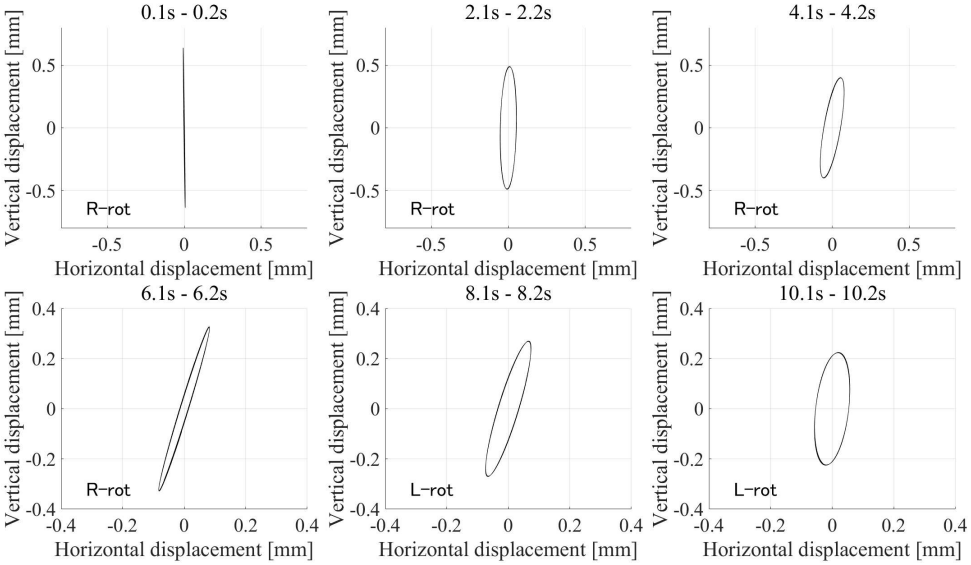



**Fig. 20** Trajectories of the fundamental of the displacement shown in Fig. 19. R-rot and L-rot indicate right and left rotations from the pianist's listening point, respectively.

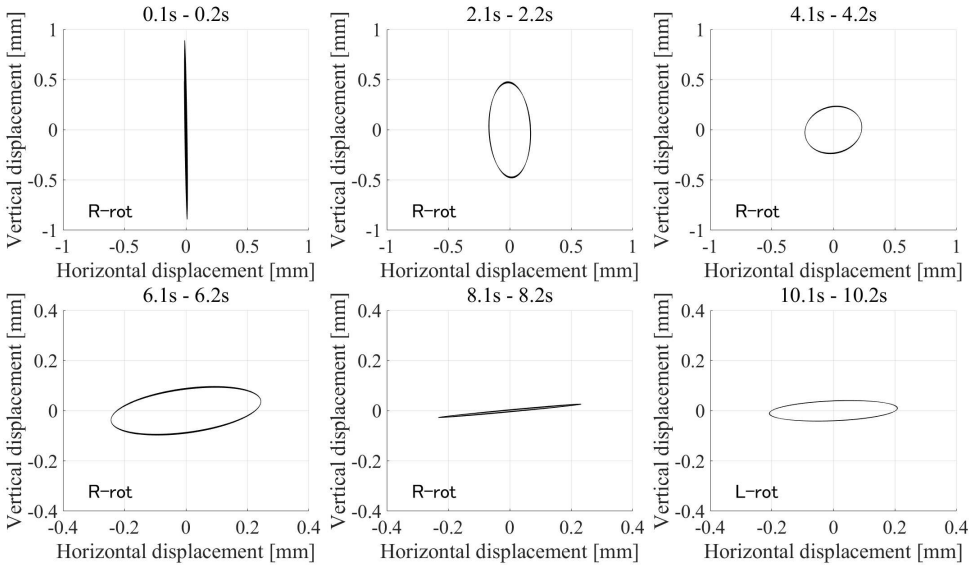



**Fig. 21** Trajectories of the second-order component shown in Fig. 19.

# 6 Conclusions

This paper introduced a physics-based, time-domain simulation framework that—unlike prior studies focusing on isolated subsystems—treats the piano as a fully integrated, three-dimensional coupled system. The model incorporates nonlinear hammer–string interaction, geometrically nonlinear string vibration with end-support anisotropy, the orthotropic complex elasticity of wood, and exterior vibroacoustics via a large-scale body–air model. By combining hybrid-interface CMS + Galerkin method for strings with FEM + FMBEM and a complex CMS based on nonlinear eigenvalue analysis for the body–air subsystem, the approach achieves substantial model-order reduction while preserving the essential dynamics required for perceptually faithful sound synthesis.

Primary contributions are threefold.

(i) System-level integration in the time domain: We simulate the complete hammer–string–body–air chain, enabling causal analysis from design parameters and manufacturing stress to radiated sound pressure.

(ii) Mechanism-faithful modeling of nonlinearities and anisotropy: A double-layer nonlinear generalized Maxwell model captures the felt hysteresis across a wide dynamic range, while geometrical nonlinearity and zig-zag/anisotropic boundary conditions at the string supports reproduce dispersion, polarization exchange, and ringing with high fidelity.

(iii) Scalable reduction for exterior vibroacoustics: The combination of FMBEM and complex CMS efficiently handles a multi-million-DOF coupled body–air problem, yielding complex modal parameters at the string support points and impulse responses to microphone positions for accurate auralization.

Perceptual validity was supported through audible examples that reconstruct salient piano phenomena—ringing, partial dispersion, and unison detuning—within a single unified physical model. These results indicate that the proposed framework can quantitatively connect specification-level choices (e.g., string support conditions, wood properties, residual stresses) and technician-level adjustments (e.g., unison tuning) to audible outcomes. As such, it provides a practical foundation for auralization-based design exploration, pedagogy, and virtual prototyping.

Limitations and scope. The present implementation neglects action mechanics in the time domain and, in the high-frequency band, ignores the feedback force exerted by air onto the body to reduce computational cost. These pragmatic choices do not alter the main conclusions but suggest clear opportunities for refinement.

Future directions. We plan to:

(i) incorporate action-mechanism dynamics (including key–hammer transfer characteristics and damper behavior) [37] into the time-domain loop;

(ii) remove the high-frequency air-to-structure feedback approximation as computational resources advance;

(iii) tighten parameter identification (e.g., loss factors, boundary anisotropy, relaxation times) via Bayesian or differential-evolution fitting against multi-modal measurements;

(iv) extend the method to other stringed instruments (e.g., guitar, violin) by reusing the same CMS-centric pipeline; and

(v) investigate real-time implementations (reduction of elements that are not auditorily dominant, maximizing parallel efficiency of the program, etc.) toward next-generation, physics-based tone generators.

In summary, this study demonstrates a numerical time-domain realization of a full-scale grand piano as a comprehensive coupled physical system. The proposed framework bridges the gap between mechanism-level modeling and perceptual evaluation, enabling reproducible, parameter-sensitive experiments that are impractical with physical prototypes alone. We anticipate that this approach will accelerate evidence-driven piano design and inform high-expressivity sound synthesis beyond conventional PCM-based methods.

**Acknowledgements.** The authors thank their colleagues at Yamaha who contributed to this study. The eigenvalue and nonlinear static analysis methods for the large-scale model using MSC Nastran were developed by Hitoshi Izutani and Makoto Minoda. Most of the Yamaha CFX measurements were performed by Junji Kuroda. A part of the signal processing algorithm in PARTITA was implemented by Onsai Ryu. The authors thank Masatsugu Okazaki for the helpful discussions on this research. One of the authors, Eiji Tominaga, thanks Takashi Tamaki, who wrote the in-house reports on experimental research into the ringing sound in 1984, and Hajime Hayashida, the former supervisor, for the opportunity to get started this research.

**Data availability.** The datasets generated and analyzed during the current study are not publicly available due to their size and proprietary restrictions, but are available from the corresponding author upon reasonable request.

**Supplementary materials.** Audio files (WAV, 44.1kHz, 24-bit, stereo) associated with this article are provided as Electronic Supplementary Material (Online Resources 1–6).

- Online Resource 1: Low range chromatic scale (Recorded sound of Yamaha CFX)
- Online Resource 2: Low range chromatic scale (Simulated sound in the case where both dispersion and geometrical nonlinearity are ignored.)
- Online Resource 3: Low range chromatic scale (Simulated sound in the case where dispersion is taken into account and geometrical nonlinearity is ignored.)
- Online Resource 4: Low range chromatic scale (Simulated sound in the case where both dispersion and geometrical nonlinearity are taken into account.)
- Online Resource 5(a): Scarlatti Sonata in E (Maximum mistuning: 2.5cent)
- Online Resource 6(a): Scarlatti Sonata in E (Perfect tuning)
- Online Resource 5(b): Chopin Fantaisie-Impromptu (Maximum mistuning: 2.5cent)
- Online Resource 6(b): Chopin Fantaisie-Impromptu (Perfect tuning)

# References

[1] Yanagisawa, T., Morioka, M., Nakamura, K., Miki, T.: Decay rate of partial

vibration of piano string under the influence of soundboard. J. Acoust. Soc. Jpn. **40**(1), 2–9 (1984). in Japanese

[2] Hall, D.E.: Piano strings excitation. VI: Nonlinear modeling. J. Acoust. Soc. Am. **92**(1), 95–105 (1992)

[3] Stulov, A.: Hysteretic model of the grand piano hammer felt. J. Acoust. Soc. Am. **97**(4), 2577–2585 (1995)

[4] Bank, B., Sujbert, L.: Generation of longitudinal vibrations in piano strings: From physics to sound synthesis. J. Acoust. Soc. Am. **117**(4), 2268–2278 (2005)

[5] Chabassier, J., Chaigne, A., Joly, P.: Modeling and simulation of a grand piano. J. Acoust. Soc. Am. **134**(1), 648–665 (2013)

[6] Marburg, S.: Modal reduction for exterior acoustic and vibroacoustic problems. J. Acoust. Soc. Am. **155**(A141) (2024)

[7] Bank, B., Avanzini, F., Borin, G., Poli, G.D., Fontana, F., Rocchesso, D.: Physically informed signal processing methods for piano sound synthesis: A research overview. EURASIP J. Adv. Signal Process **2003**(464536) (2003)

[8] Kunio, T.: Fundamentals of Solid Mechanics, pp. 237–251. Baifukan, in Japanese (1977)

[9] Nakamura, I., Naganuma, D.: Characteristics of piano sound spectra. in Proc. Stockholm Music Acoust. Conf., 325–330 (1993)

[10] Ellis, J.: Longitudinal modes in piano strings: Results of new research. Piano Technichians Journal (5), 16–23 (1998)

[11] Chaigne, A., Chabassier, J., Burban, N.: Acoustics of pianos: physical modeling, simulations and experiments. Proceedings of the Stockholm Music Acoustics Conference, SMAC 2013, Stockholm, Sweden, 585–592 (2013)

[12] Tan, J.J.: Piano acoustics: string's double polarization and piano source identification. Ph.D. dissertation, University Paris-Saclay (2017)

[13] Kondo, K.: Vibration Theory, pp. 159–180. Baifukan, in Japanese (1993)

[14] Leissa, A.W., Saad, A.M.: Large amplitude vibrations of strings. Trans.ASME.J. Appl. Mech. **61**(2), 296–301 (1994)

[15] Kosmatka, J.B.: Damping behavior of initially-stressed beams. Collect Tech Pap AIAA/ASME/ASCE/AHS/ASC Struct Struct Dyn Mater Conf **49**(7), 4545–4555 (2008)

[16] Lesieutre, G.A.: How membrane loads influence the modal damping of flexural

structures. Collect Tech Pap AIAA/ASME/ASCE/AHS/ASC Struct Struct Dyn Mater Conf **49**(9), 5835–5843 (2008)

[17] Fletcher, N.H., Rossing, T.D.: The Physics of Musical Instruments 2nd Ed. Springer, New York (1998). Chap. 2

[18] Nagamatsu, A.: Modal Analysis, pp. 49–52. Baifukan, in Japanese (1985)

[19] Kobayashi, S.: Vibrationology, pp. 174–190. Maruzen, in Japanese (1994)

[20] Murase, Y., Sawada, S.: Polymer materials in application to sound I. Polymers **37**(5), 392–393 (1988). in Japanese

[21] MSC Nastran 2025.1 Nonlinear (SOL 400) User's Guide

[22] Yasuda, Y.: Study on large-scale sound field analysis using fast multipole boundary element method. Ph.D. dissertation, The University of Tokyo (2003). in Japanese

[23] Gumerov, N.A., Duraiswami, R.: Fast Multipole Methods for the Helmholtz Equation in Three Dimensions, ELSEVIER (2004)

[24] Yasuda, Y., Sakuma, T.: Computational Simulation in Architectural and Environmental Acoustics - Methods and Applications of Wave-Based Computation, Springer (2014). Chap. 4

[25] Williams, E.G.: Fourier Acoustics - Sound Radiation and Nearfield Acoustical Holography, ELSEVIER (1999). Chap. 6

[26] Suzuki, S., Imai, M., Ishiyama, S.: Coupling of the boundary element method and modal analysis for structural acoustic problems. Trans. Jpn. Soc. Mech. Eng. C **52**(473), 310–317 (1986). in Japanese

[27] Yokota, S., Sakurai, T.: A projection method for nonlinear eigenvalue problems using contour integrals. JSIAM Lett **5**, 41–44 (2013)

[28] Xiao, J., Menga, S., Zhang, C., Zheng, C.: Resolvent sampling based rayleigh-ritz method for large-scale nonlinear eigenvalue problems. Comput. Methods Appl. Mech. Eng. **310**, 33–57 (2016)

[29] Xiao, J., Zhang, C., Huang, T.M., Sakurai, T.: Solving large-scale nonlinear eigenvalue problems by rational interpolation approach and resolvent sampling based rayleigh-ritz method. Int. J. Numer. Meth. Eng. **110**(8), 776–800 (2017)

[30] Xiao, J., Wang, J., Liang, T., Wen, L.: The RSRR method for solving large-scale nonlinear eigenvalue problems in boundary element method. Engineering Analysis with Boundary Elements **93**, 150–160 (2018)

[31] Liang, T., Wang, J., Xiao, J., Wen, L.: Coupled BE-FE based vibroacoustic modal analysis and frequency sweep using a generalized resolvent sampling method. Comput. Methods Appl. Mech. Engrg. **345**, 518–538 (2019)

[32] Nagamatsu, A.: Modal Analysis, pp. 76–85. Baifukan, in Japanese (1985)

[33] Das, S., Suganthan, P.N.: Differential evolution: A survey of the state-of-the art. IEEE Trans. on Evolutionary Computation **15**(1), 4–31 (2011)

[34] Y. Kubojima, M.O. H. Yoshihara, Okano, T.: Examination of the method of measuring the shear modulus of wood based the Timoshenko theory of bending. Mokuzai Gakkaishi **42**(12), 1170–1176 (1996)

[35] Podlesak, M., Lee, A.R.: Dispersion of waves in piano strings. J. Acoust. Soc. Am. **83**, 305–317 (1988)

[36] Tanaka, H., Nagai, K., Mizutani, K.: Measurement of two-dimensional vibration of piano strings. J. Acoust. Soc. Jpn. **56**(3), 148–155 (2000). in Japanese

[37] Tominaga, E., Sato, T.: Physical modeling and simulation of piano touch. J. Jpn. Soc. Tribologists **62**(10), 623–628 (2017). in Japanese

## Supplementary Files

This is a list of supplementary files associated with this preprint. Click to download.

- OnlineResource2.wav
- OnlineResource3.wav
- OnlineResource4.wav
- OnlineResource1.wav
- OnlineResource5b.wav
- OnlineResource5a.wav
- OnlineResource6a.wav
- OnlineResource6b.wav